Supplementary Information

Efficient hydrogen evolution at Ni/CeO_x interfaces in anion-exchange membrane water electrolysers

Ibrahem O. Baibars[1], Haisen Huang[2], Yang Xiao[1], Shuhao Wang[1], Yan Nie[1], Chen Jia[1], Kamran Dastafkan[1], and Chuan Zhao*[1]

[1]School of Chemistry, Faculty of Science, University of New South Wales (UNSW)

[2]CAS Key Laboratory of Materials for Energy Conversion, Department of Materials Science and Engineering, University of Science and Technology of China, Hefei, Anhui, 230026, P.R. China.

*Corresponding author: chuan.zhao@unsw.edu.au

Calculation methods

Potential conversion

All potentials reported for half cells are measured vs. calibrated Saturated Calomel Electrode (SCE) but reported vs. the reversible hydrogen electrode (RHE), following equation S1.

$$E_{\mathrm{RHE}} = E_{SCE} + 0.241 + 0.059\ \mathrm{pH} \qquad \text{(S1)}$$

Deposition faradaic efficiency

The faradaic efficiencies of the deposition processes are determined by separate calculations of the electric charges consumed in the deposition of Ni (Q_{Ni}) and CeO$_x$ ($Q_{\mathrm{CeO_x}}$) relative to the total applied charge, according to equation S2. The remaining charge, other than that used in film deposition, is described as hydrogen evolution charge, where other competing reactions, such as oxygen and nitrate reduction, have minimal contribution due to their low concentrations involved.

$$Faradaic\ efficency\ \% = \frac{Q_{\mathrm{Ni}} + Q_{\mathrm{CeO_x}}}{Q_{\mathrm{total}}} \times 100 \qquad \text{(S2)}$$

where Q_{Ni} and $Q_{\mathrm{CeO_x}}$ are calculated from the masses measured by ICP-OES according to equations S3 and S4.

$$Q_{\mathrm{N}i} = \frac{m_{\mathrm{Ni}} \times n \times F}{Atomic\ mass_{\mathrm{Ni}}} = \frac{m_{\mathrm{Ni}} \times 2 \times 96485}{58.69} \qquad \text{(S3)}$$

$$Q_{\mathrm{CeO_x}} = \frac{m_{\mathrm{Ce}} \times n \times F}{Atomic\ mass_{\mathrm{Ce}}} = \frac{m_{\mathrm{Ce}} \times 1 \times 96485}{140.12} \qquad \text{(S4)}$$

where *F* represents Faraday's constant, *m* is the mass in grams of each respective element, and n denotes the number of electrons involved in the deposition process, which is 2 in case of Ni^{2+} (solution) to Ni^0 (catalyst) conversion, see equation S5, and considered 1 in case of CeO$_x$ deposition, see equations S6-S8.

$$Ni^{2+} + 2\ e^{-} \rightarrow Ni \qquad \text{(S5)}$$

The deposition mechanism of CeO_2 from Ce^{3+} ions is controversial, being an oxidative deposition happening at the cathode. Herein, the H_2O_2-mediated deposition mechanism is adopted, where a chemical deposition occurs via H_2O_2 molecules (equation S7), which are electrochemically generated from dissolved O_2 reduction at the cathode (equation S6), with H_2O_2 acting as an oxidising and reducing agent, respectively, in a mediation process [1]. This may explain the very low faradaic efficiency (0.37%) observed for CeO$_x$ deposition, bearing in mind that dissolved O_2 is a limiting reactant. The absence of macroporosity in the CeO_x film could be explained via this mechanism by considering the slow rate of particle growth (due to the lack of vicinal O_2) around the formed hydrogen bubbles that evolve rapidly before hollow cone-shaped morphologies can be built.

$$O_2 + 2\,e^- + 2\,H_2O \rightarrow H_2O_2 + 2\,OH^- \qquad \text{(S6)}$$

$$H_2O_2 + 6\,OH^- + 2\,Ce^{3+} \rightarrow 2\,CeO_2 + 4\,H_2O \qquad \text{(S7)}$$

$$2\,Ce^{3+} + O_2 + 4\,OH^- + 2\,e^- \rightarrow 2\,CeO_2 + 2\,H_2O \qquad \text{(Overall, S8)}$$

Tafel slopes and exchange current densities

Linear fittings of the charge-transfer-controlled linear regions of Tafel plots to Tafel equation (S9) are used to determine both Tafel slopes and exchange current densities from slopes and intercepts, respectively [2].

$$|\eta| = b\log|i| - b\log|i_0| \qquad \text{(S9)}$$

where η is the measured overpotential in (V), i is the measured current density in (A cm^{-2}), b is Tafel slope ($\frac{2.303\times RT}{\alpha nF}$), and i_0 is the exchange current density in (A cm^{-2}).

ECSA and C_{dl} calculations

Values of the electrochemical active surface area (*ECSA*) are calculated in (cm^2) and reported in cm^2_{ECSA}/cm^2_{geo} as they are measured over 1 cm^2_{geo} substrates. These values are calculated from the corresponding double-layer capacitance (C_{dl}) of the film, according to equation S10.

$$ECSA = \frac{C_{dl}}{C_s} \qquad \text{(S10)}$$

where C_s is the specific capacitance, which is reported in the literature to equal 0.04 (mF cm^{-2}_{ECSA}) in 1.0 M OH^- solutions [3–5]. On the other hand, C_{dl} values are figured from the measured slopes of the linear variations of capacitive current at a certain potential with the applied potential scan rate, according to equation S11.

$$I = C_{dl} \times \frac{dE}{dt} \qquad \text{(S11)}$$

where C_{dl} comes in (mF) when I (the capacitive current) is in (A) and $\frac{dE}{dt}$ (the scan rate) is in (mV s^{-1}). The gravimetric-specific $ECSA$ values are calculated per (mg) of the deposited catalyst according to equation S12.

$$Specific\ ECSA = \frac{ECSA}{m} \qquad \text{(S12)}$$

where m is the mass of the deposited film in mg.

TOF calculations

Turnover frequency (*TOF*) values, the number of hydrogen molecules generated per second per active site, are calculated following equation S13.

$$TOF = \frac{I_{\mathrm{H_2}} \times N_{\mathrm{A}}}{x \times n_{\mathrm{H_2}} \times F} \qquad \text{(S13)}$$

where $I_{\mathrm{H_2}}$ is the HER current in (A), N_{A} is Avogadro's constant, $n_{\mathrm{H_2}}$ is the number of electrons consumed in the production of one molecule of H_2, which is 2, F is Faraday's constant, and x is the number of active sites, which is calculated from the corresponding redox CV of each film, according to equation S14.

$$x = \frac{Q_{\mathrm{CV}} \times N_{\mathrm{A}}}{n_{\mathrm{CV}} \times F} \qquad \text{(S14)}$$

where Q_{CV} is the charge associated with each CV in (C), and n_{CV} is the number of electrons involved in the processes during the CV, which is 2. Therefore, equation S13 can be simplified to equation S15.

$$TOF = \frac{I_{\mathrm{H_2}}}{Q_{\mathrm{CV}}} = \frac{I_{\mathrm{H_2}} \times (dE/dt)_{\mathrm{CV}}}{(\int I\, dE)_{\mathrm{CV}}} \qquad \text{(S15)}$$

Where $(dE/dt)_{\mathrm{CV}}$ is the potential scan rate used for CV in (V s^{-1}), and $(\int I\, dE)_{\mathrm{CV}}$ is the area enclosed by the CV in (A V) calculated by integration.

Energy efficiency in AEMWE

The values of energy efficiency are dependent on the operating current density, the associated cell voltage, and the heating value of hydrogen. These values are calculated, according to equation S16&S17, based on the higher heating value (*HHV,* 285.8 kJ mol^{-1}) and the lower heating value (LHV, 241.8 kJ mol^{-1}) of hydrogen gas [6], respectively.

$$HHV\ Energy\ efficiency = \frac{HHV \text{ of } \mathrm{H_2}}{Consumed\ electricity} \times 100 = \frac{285.8\ (\mathrm{kJ\ mol^{-1}}) \times 100}{nFE_{\mathrm{cell}}}$$
$$= \frac{285.8\ (\mathrm{kJ\ mol_{H_2}^{-1}}) \times 100}{2\left(\mathrm{mol_{e}\text{-}\ mol_{H_2}^{-1}}\right) \times 96485(\mathrm{C\ mol_{e^-}^{-1}}) \times E_{\mathrm{cell}}}$$
$$= \frac{1.481\ (\mathrm{V})}{E_{\mathrm{cell}}\ (\mathrm{V})} \times 100 \qquad \text{(S16)}$$

$$LHV\ Energy\ efficiency = \frac{LHV \text{ of } \mathrm{H_2}}{Consumed\ electricity} \times 100 = \frac{241.8\ (\mathrm{kJ\ mol^{-1}}) \times 100}{nFE_{\mathrm{cell}}}$$
$$= \frac{241.8\ (\mathrm{kJ\ mol_{H_2}^{-1}}) \times 100}{2\left(\mathrm{mol_{e}\text{-}\ mol_{H_2}^{-1}}\right) \times 96485\ (\mathrm{C\ mol_{e^-}^{-1}}) \times E_{\mathrm{cell}}}$$
$$= \frac{1.253\ (\mathrm{V})}{E_{\mathrm{cell}}\ (\mathrm{V})} \times 100 \qquad \text{(S17)}$$

where *n* is the number of moles of electrons consumed to produce a mole of hydrogen gas, *F* denotes Faraday's constant, and E_{cell} is the operating cell voltage.

Electrical efficiency in AEMWE

The amount of electrical energy consumed to produce 1 kg of hydrogen is also dependent on the operating current density (rate of production) and the corresponding cell voltage, equation S18.

$$\text{Electrical Efficiency} = \frac{\text{Electrical Energy}}{\text{Mass of produced Hydrogen}} = \frac{E_{\mathrm{cell}}It}{\frac{ItM}{nF}} = \frac{E_{\mathrm{cell}}nF}{M}$$
$$= \frac{E_{\mathrm{cell}}\ (\mathrm{V}) \times 2\left(\mathrm{mol_{e}\text{-}\ mol_{H_2}^{-1}}\right) \times 96485\ (\mathrm{C\ mol_{e^-}^{-1}})}{2\ (\mathrm{g\ mol_{H_2}^{-1}})} \times \frac{1000\ (\mathrm{g})}{1\ (\mathrm{kg})} \times \frac{1\ (\mathrm{kWh})}{3.6 \times 10^{6}\ (\mathrm{C\ V})}$$
$$= E_{\mathrm{cell}}\ (\mathrm{V}) \times 26.801\ (\mathrm{kWh\ kg^{-1}\ V^{-1}}) \qquad \text{(S18)}$$

where *M* is the molar mass of hydrogen gas, *n* is the number of moles of electrons consumed to produce a mole of hydrogen gas, *F* denotes Faraday's constant, *t* denotes the time of operation, while *I* and E_{cell} are the operating current and cell voltage.

Cost of H_2 from AEMWE

Hydrogen cost is calculated based on the electrical efficiency in AEMWE and the electricity price (0.02 \$ kWh^{-1} [7]), according to equation S19.

$$\begin{aligned}\text{Cost of } \mathrm{H_2}(\$\ \mathrm{kg^{-1}}) &= \text{Electrical Efficiency } (\mathrm{kWh\ kg^{-1}}) \times \text{Electricity price } (\$\ \mathrm{kWh^{-1}}) \\ &= \text{Electrical Efficiency } (\mathrm{kWh\ kg^{-1}}) \times 0.02\ (\$\ \mathrm{kWh^{-1}}) \qquad \text{(S19)}\end{aligned}$$

Faradaic efficiency in AEMWE

The amount of H_2 produced by AEMWE is determined by gas chromatography (GC, Shimadzu GC 2010), where 1.0 M KOH is circulated from the anode side, while Ar gas is circulated at a specific flow rate (υ) from the cathode side carrying H_2 gas in an online setup into the GC. The faradaic efficiency is calculated according to equation S20.

$$Faradaic\ efficiency\ \% = \frac{moles \text{ of } \mathrm{H_2}}{Theoretical\ moles \text{ of } \mathrm{H_2}} \times 100\% = \frac{\left(\frac{PV}{RT}\right)_{\mathrm{H_2}}}{\frac{It}{nF}} \times 100\%$$

$$= \frac{\left(\frac{PV}{RT}\right)_{\mathrm{H_2}} / V_{\mathrm{total}}}{\left(\frac{It}{nF}\right) / V_{\mathrm{total}}} \times 100\% = \frac{\left(\frac{PV\%}{RT}\right)_{\mathrm{H_2}} \times \upsilon}{\left(\frac{I}{nF}\right)}$$

$$= \frac{0.1316\ \left(\frac{\mathrm{min.A}}{\mathrm{ml}},\ \text{at } 25\ ^{\circ}\mathrm{C}\right) \times V\%_{\mathrm{H_2}} \times \upsilon\ \left(\frac{\mathrm{ml}}{\mathrm{min}}\right)}{I\ (\mathrm{A})} \qquad (S20)$$

Where $V\%_{\mathrm{H_2}}$ is the volume percentage of H_2 in the Ar and H_2 mixture, υ is the gas flow rate in ml/min, and I is the applied current in A.

IR and Mass-transfer free LSVs

To deconvolute the observed overpotential at the full cell and the AEMWE into its three originating types: ohmic, mass transfer, and activation, the following strategy is adopted. Firstly, raw LSV data are measured and depicted without *IR* compensation. Secondly, the *IR*-corrected LSV is drawn, where the difference between the two curves is the *IR* drop. Thirdly, the activation drop is calculated by the extension of the *IR*-compensated Tafel plot, which is measured at the activation-controlled region, to the high-current-density mass-transfer-controlled region, according to equation S21 [8]. Thereby, an activation-controlled, mass-transfer-free and *IR*-free LSV is drawn.

$$|E_{IR \text{ and Mass free}}| = |E_{\mathrm{Thermo}}| + \eta_{\mathrm{activation}} = |E_{\mathrm{Thermo}}| + b \log i - b \log i_0 \qquad \text{(S21)}$$

where $E_{IR \text{ and Mass free}}$ is the *IR* and mass-transfer-free potential, which is drawn vs *i,* the raw measured current density, to construct the activation-controlled LSV. E_{Thermo} denotes the thermodynamic potential of water electrolysis at 60 °C, which equals −1.199 V. b and $-b \log i_0$ are Tafel slope and Tafel intercept, respectively. Finally, the mass transfer overpotential is considered as the drop between the *IR*-corrected and activation-controlled LSVs.

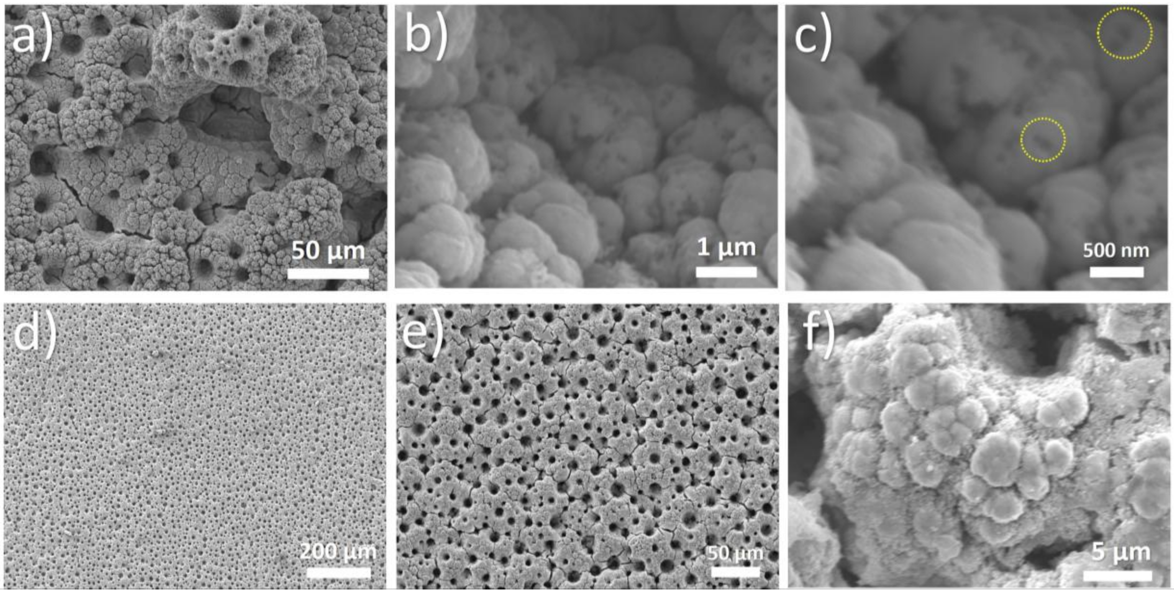

Fig. S1. SEM micrographs of the Ni/CeO_x (2 A) film over Ni foam (a-c), over Al foil (d-f) at different magnifications.

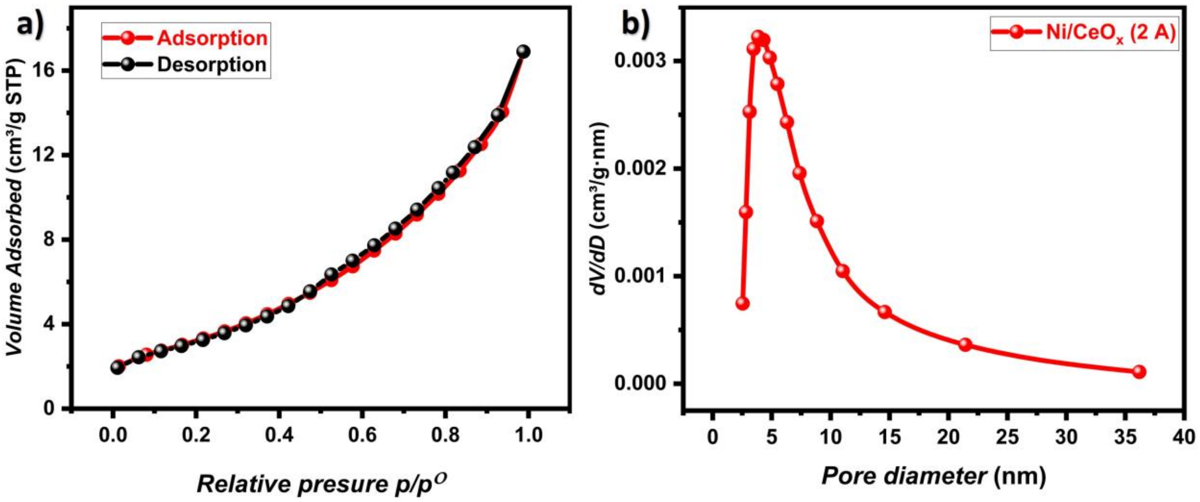

Fig. S2. a) N_2 adsorption/desorption (BET) isotherm and b) pore size distribution of the Ni/CeO$_x$ (2 A) film.

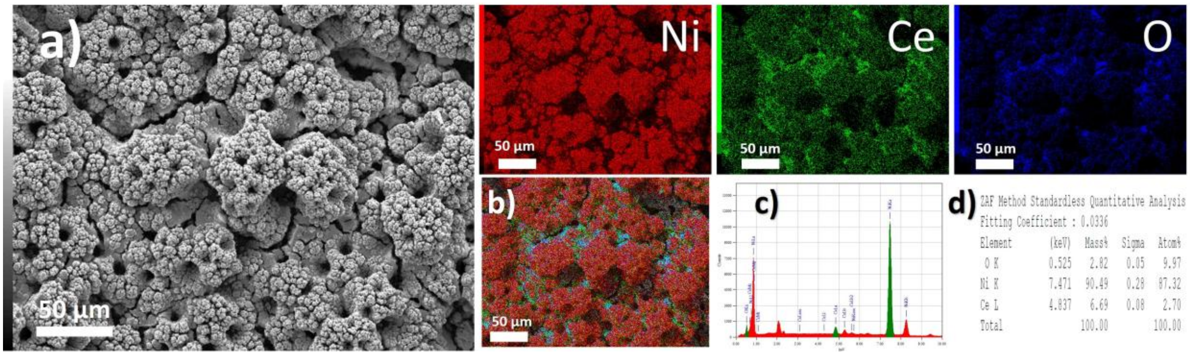

```
ZAF Method Standardless Quantitative Analysis
Fitting Coefficient : 0.0336
Element          (keV)   Mass%   Sigma   Atom%
 O K             0.525    2.82    0.05    9.97
Ni K             7.471   90.49    0.28   87.32
Ce L             4.837    6.69    0.08    2.70
Total                   100.00          100.00
```

Fig. S3. a) SEM micrograph of the Ni/CeO$_x$ (2 A) film and the corresponding EDS elemental mapping, b) overlay, c) spectra, and d) percentages.

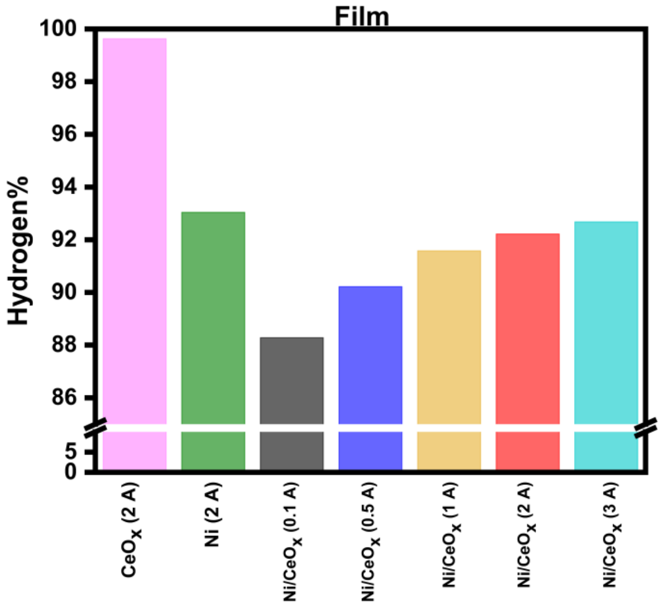

Fig. S4. Percentage of the charge consumed, according to the ICP-OES data, in generating hydrogen gas during electrodeposition.

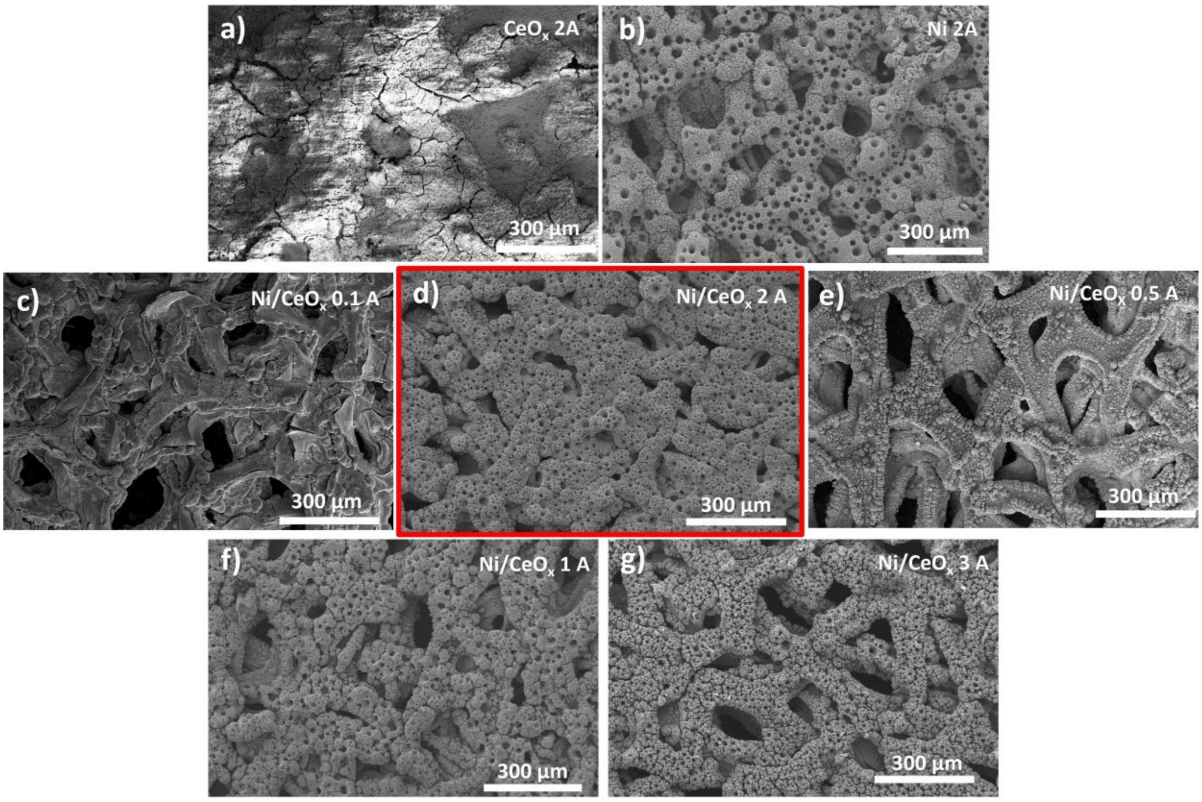

Fig. S5. SEM micrographs of a) CeO$_x$ (2 A), b) Ni (2 A), c) Ni/CeO$_x$ (0.1 A), d) Ni/CeO$_x$ (2 A), e) Ni/CeO$_x$ (0.5 A), f) Ni/CeO$_x$ (1 A), and g) Ni/CeO$_x$ (3 A) films.

Note S1:

For comparison, in the absence of either Ni^{2+} or Ce^{3+}, CeO$_x$ and Ni films are deposited, respectively, at 2 A cm^{-2} (Fig. S5). The CeO$_x$ film appears yellowish-white in colour, matching the colour reported for the non-stochiometric CeO_2 material [9], while Ni and Ni/CeO$_x$ films appear brownish-black (Fig. S6). As expected, the CeO$_x$ catalyst shows no uniform porosity but a tortuously grown layer with in-between cracks, similar to the morphology reported in the literature for electrodeposited CeO_2 [10], supporting the unsuitability of the employed deposition bath and technique (DHBT) for building macroporous Ce films (Fig. S7). SEM-EDS of the CeO$_x$ catalyst shows a uniform distribution of Ce and O along the film, supporting the formation of cerium oxides (Fig. S7). The deposition faradaic efficiency is 0.37% only, i.e., most of the passing charge is evolving hydrogen gas.

Conversely, the deposited Ni catalyst exhibits the typical macroporous morphology expected, with relatively wider macropores, compared to the Ni/CeO$_x$ (2 A) film, with diameters spanning from 52 µm to 140 nm, (Fig. S5&8). This implies a higher tendency for the generation of larger bubbles in the absence of Ce ions during deposition. Hydrogen generation consumes 93.04% of the passing charge during the deposition, according to ICP-OES data. Ni film particles are cauliflower-like with minimal O content (2.5 atomic%), see SEM-EDS data in Fig. S8, likely due to oxidation of the top surface of Ni by atmospheric air [11,12]. This data confirms the successful formation of Ni in metallic form by the employed synthesis strategy.

For Ni/CeO$_x$ films, notable distinctions in morphologies are observed when different deposition current densities are applied (Fig. S5). Ni/CeO$_x$ (0.1 A) film lacks porosity, closely resembling the morphology of the CeO$_x$ film (Fig. S9). This implies that the bubble generation rate at this current density is insufficient to create macropores or prevent particle growth and linkage. The elemental distribution maps from SEM-EDS reveal that O sites surround Ce sites, endorsing the formation of cerium oxides. As for Ni/CeO_x (0.5 A), the morphology still lacks porosity with several small cauliflower-like particles dominating, similar to those observed for Ni film (Fig. S10). The overlaid SEM-EDS distribution of elements discloses the consistent coexistence of Ce and O, aligning with observations from the other films. Conversely, macropores begin to emerge with Ni/CeO_x (1 A). These macropores (Fig. S11) are fewer and wider than those observed for Ni/CeO_x (2 A), reflecting the lower rate of hydrogen evolution during deposition. In contrast, a higher number of narrower macropores are observed for Ni/CeO_x (3 A) due to the higher rate of hydrogen bubbling (Fig. S12). SEM-EDS data for both Ni/CeO_x (1 A) and (3 A) confirm the convergence of Ce and O.

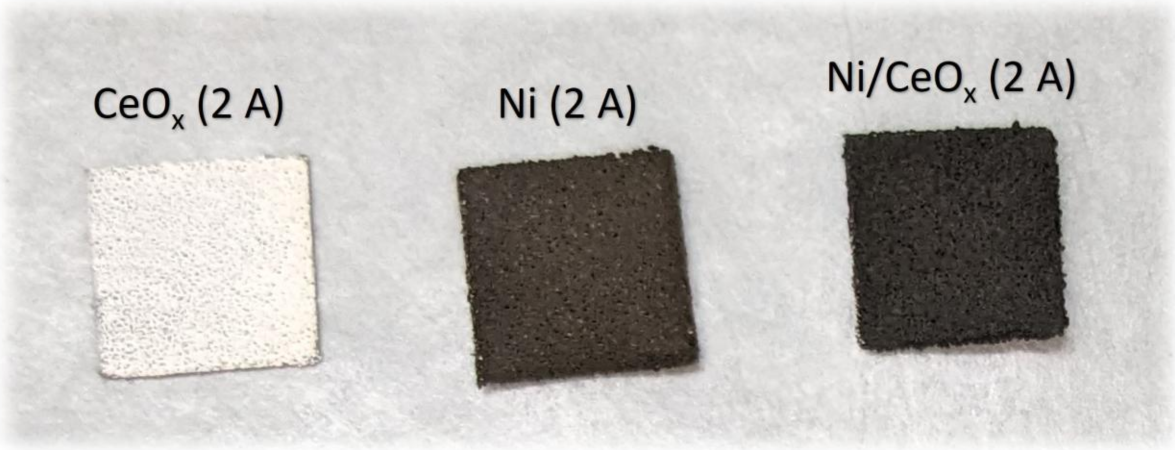

Fig. S6. Photos of CeO$_x$ (2 A), Ni (2 A), and Ni/CeO$_x$ (2 A) films.

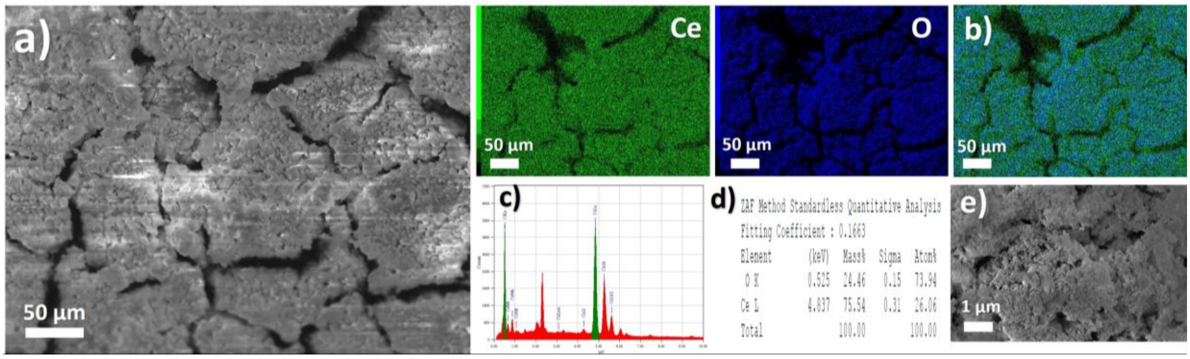

ZAF Method Standardless Quantitative Analysis
Fitting Coefficient : 0.1663

Element	(keV)	Mass%	Sigma	Atom%
O K	0.525	24.46	0.15	73.94
Ce L	4.837	75.54	0.31	26.06
Total		100.00		100.00

Fig. S7. a) SEM micrograph and the corresponding EDS elemental mapping, b) overlay, c) spectra, d) percentages, and e) magnified SEM micrograph of the CeO_x (2 A) film.

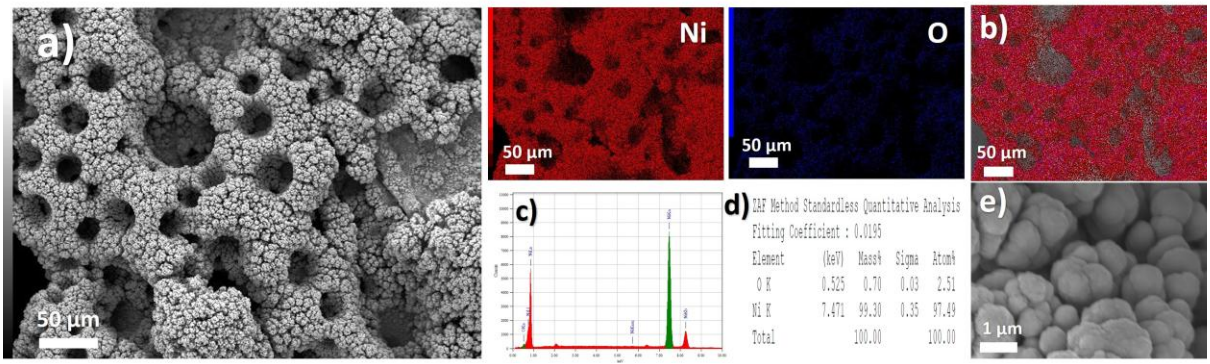

ZAF Method Standardless Quantitative Analysis
Fitting Coefficient : 0.0195

Element	(keV)	Mass%	Sigma	Atom%
O K	0.525	0.70	0.03	2.51
Ni K	7.471	99.30	0.35	97.49
Total		100.00		100.00

Fig. S8. a) SEM micrograph and the corresponding EDS elemental mapping, b) overlay, c) spectra, d) percentages, and e) magnified SEM micrograph of the Ni (2 A) film.

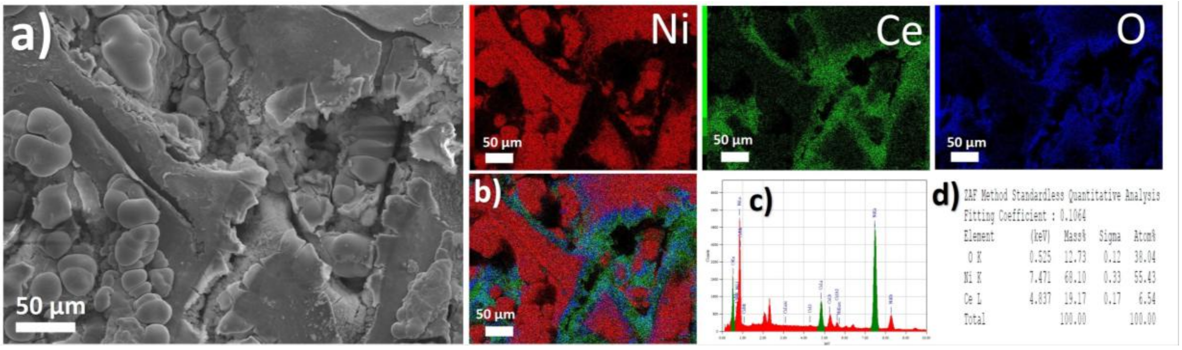

```
ZAF Method Standardless Quantitative Analysis
Fitting Coefficient : 0.1064
Element          (keV)   Mass%   Sigma   Atom%
 O K             0.525   12.73    0.12   38.04
Ni K             7.471   68.10    0.33   55.43
Ce L             4.837   19.17    0.17    6.54
Total                   100.00          100.00
```

Fig. S9. a) SEM micrograph of the Ni/CeO$_x$ (0.1 A) film and the corresponding EDS elemental mapping, b) overlay, c) spectra, and d) percentages.

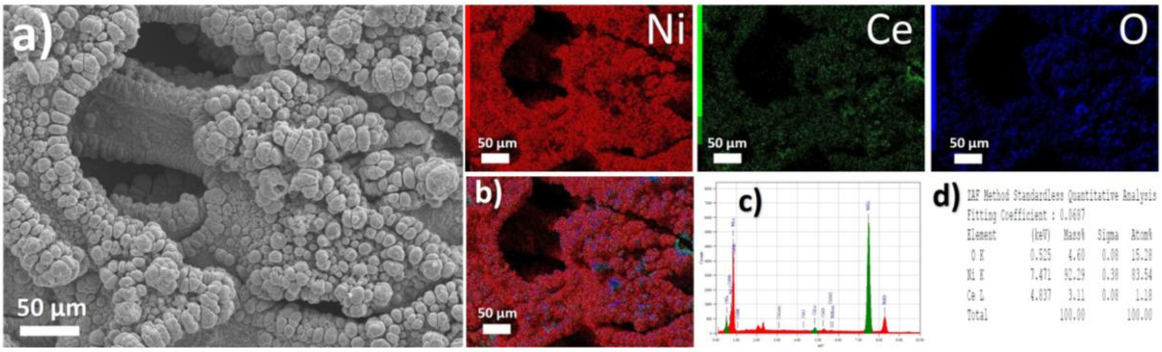

ZAF Method Standardless Quantitative Analysis
Fitting Coefficient : 0.0687

Element	(keV)	Mass%	Sigma	Atom%
O K	0.525	4.60	0.08	15.28
Ni K	7.471	92.29	0.38	83.54
Ce L	4.837	3.11	0.08	1.18
Total		100.00		100.00

Fig. S10. a) SEM micrograph of the Ni/CeO$_x$ (0.5 A) film and the corresponding EDS elemental mapping, b) overlay, c) spectra, and d) percentages.

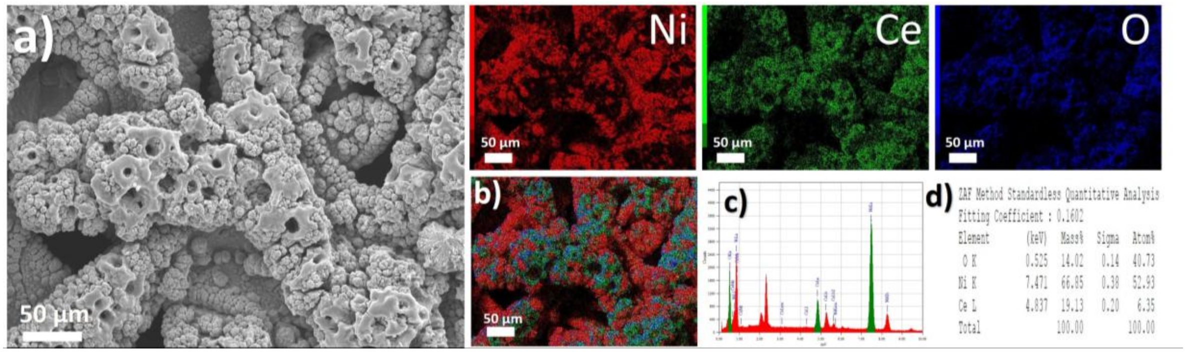

```
ZAF Method Standardless Quantitative Analysis
Fitting Coefficient : 0.1602
Element        (keV)  Mass%  Sigma  Atom%
 O K           0.525  14.02   0.14  40.73
Ni K           7.471  66.85   0.38  52.93
Ce L           4.837  19.13   0.20   6.35
Total                100.00        100.00
```

Fig. S11. a) SEM micrograph of the Ni/CeO$_x$ (1 A) film and the corresponding EDS elemental mapping, b) overlay, c) spectra, and d) percentages.

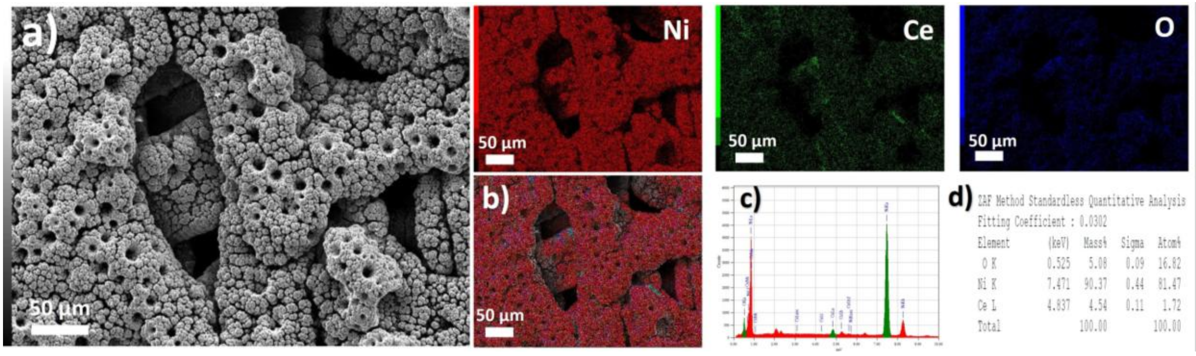

```
ZAF Method Standardless Quantitative Analysis
Fitting Coefficient : 0.0302
Element         (keV)   Mass%   Sigma   Atom%
 O K            0.525    5.08    0.09   16.82
Ni K            7.471   90.37    0.44   81.47
Ce L            4.837    4.54    0.11    1.72
Total                  100.00          100.00
```

Fig. S12. a) SEM micrograph of the Ni/CeO$_x$ (3 A) film and the corresponding EDS elemental mapping, b) overlay, c) spectra, and d) percentages.

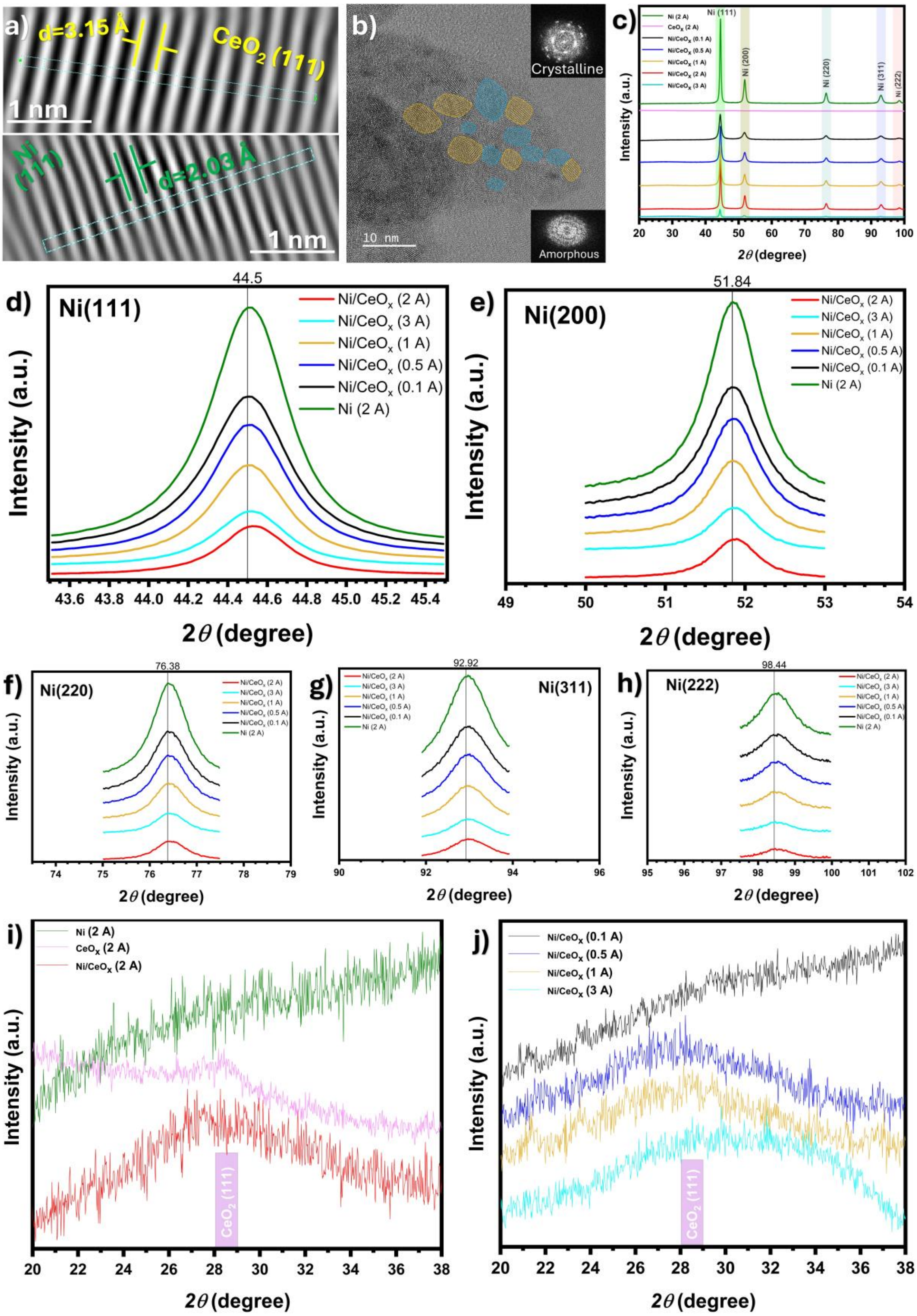

Fig. S13. a) Inverse FFT images of the (111) facets of both cubic Ni and cubic CeO_x in Ni/CeO_x (2 A). b) Crystalline (orange) and amorphous (blue) regions in HRTEM image of Ni/CeO_x (2 A), insets show the FFT patterns of both regions. c) XRD patterns. d-j) Zoomed XRD patterns of the designed Ni/CeO_x, Ni, CeO_x films.

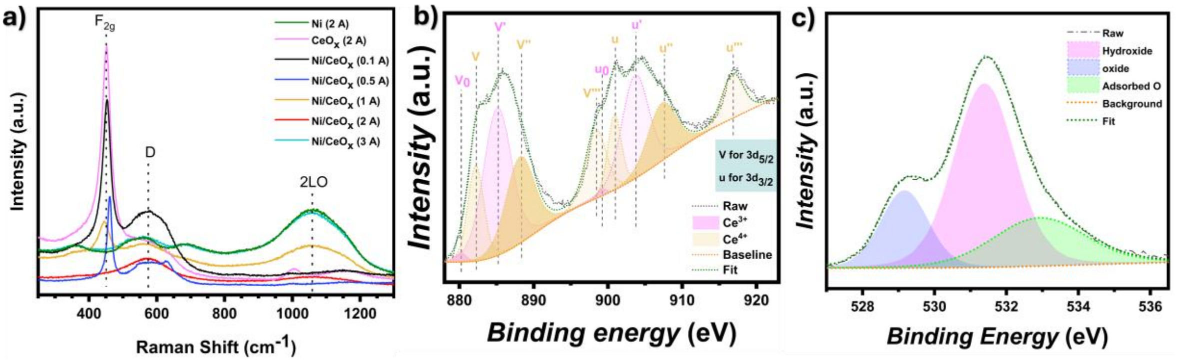

Fig. S14. a) Raman spectra of the designed Ni/CeO$_x$, Ni, CeO$_x$ films. b-c) XPS spectra of the CeO$_x$ (2 A) film: b) Ce 3d spectra and c) O 1s spectra.

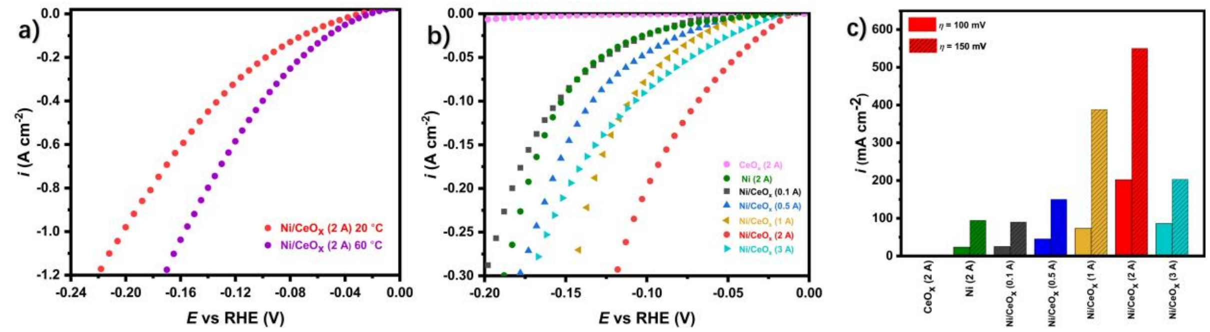

Fig. S15. a) HER LSVs of Ni/CeO$_x$ (2 A) at 20 and 60 °C. b) HER LSVs of the deposited films at 20 °C. c) HER current densities of the deposited films at 100 and 150 overpotentials at 20 °C.

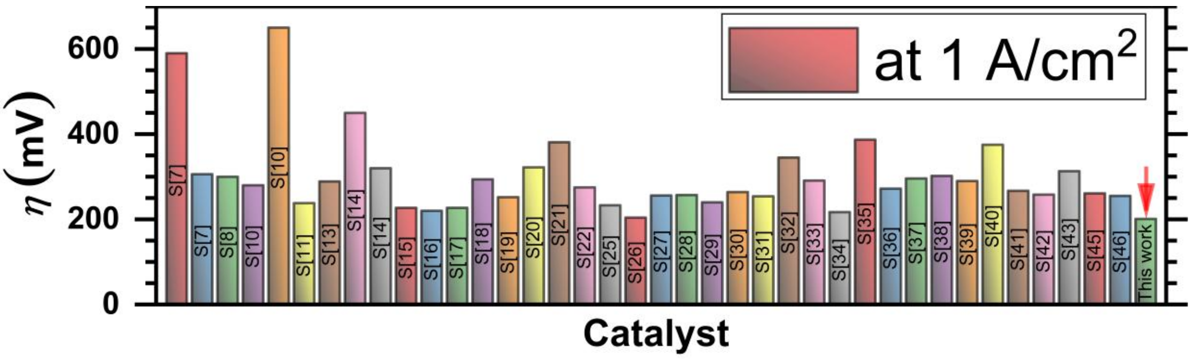

Fig. S16. Comparison between η_{1000} for HER electrocatalysts in 1 M KOH.

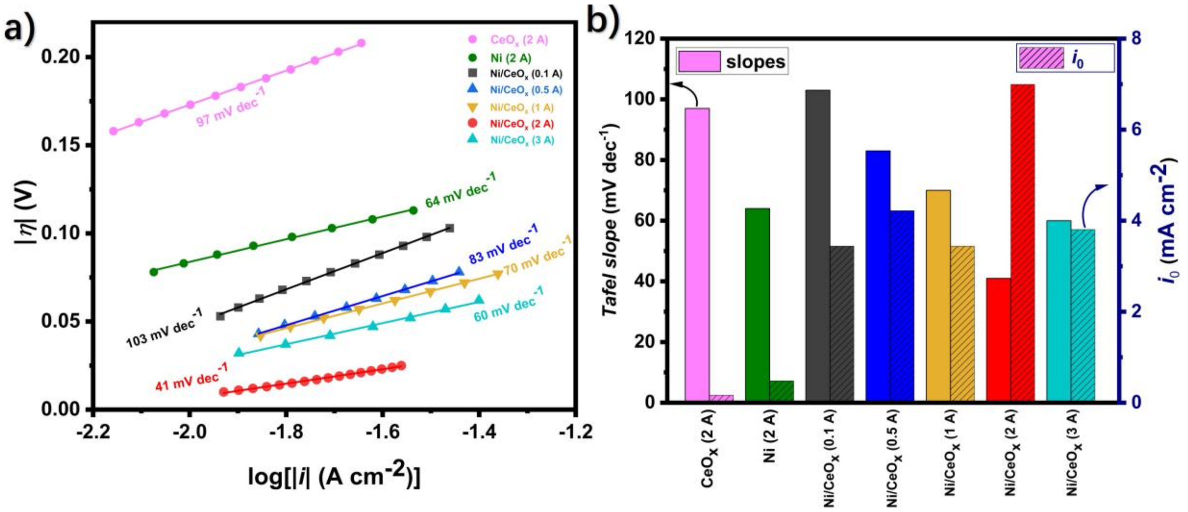

Fig. S17. a) Tafel plots of the deposited films. b) Tafel slopes and exchange current densities of the deposited films.

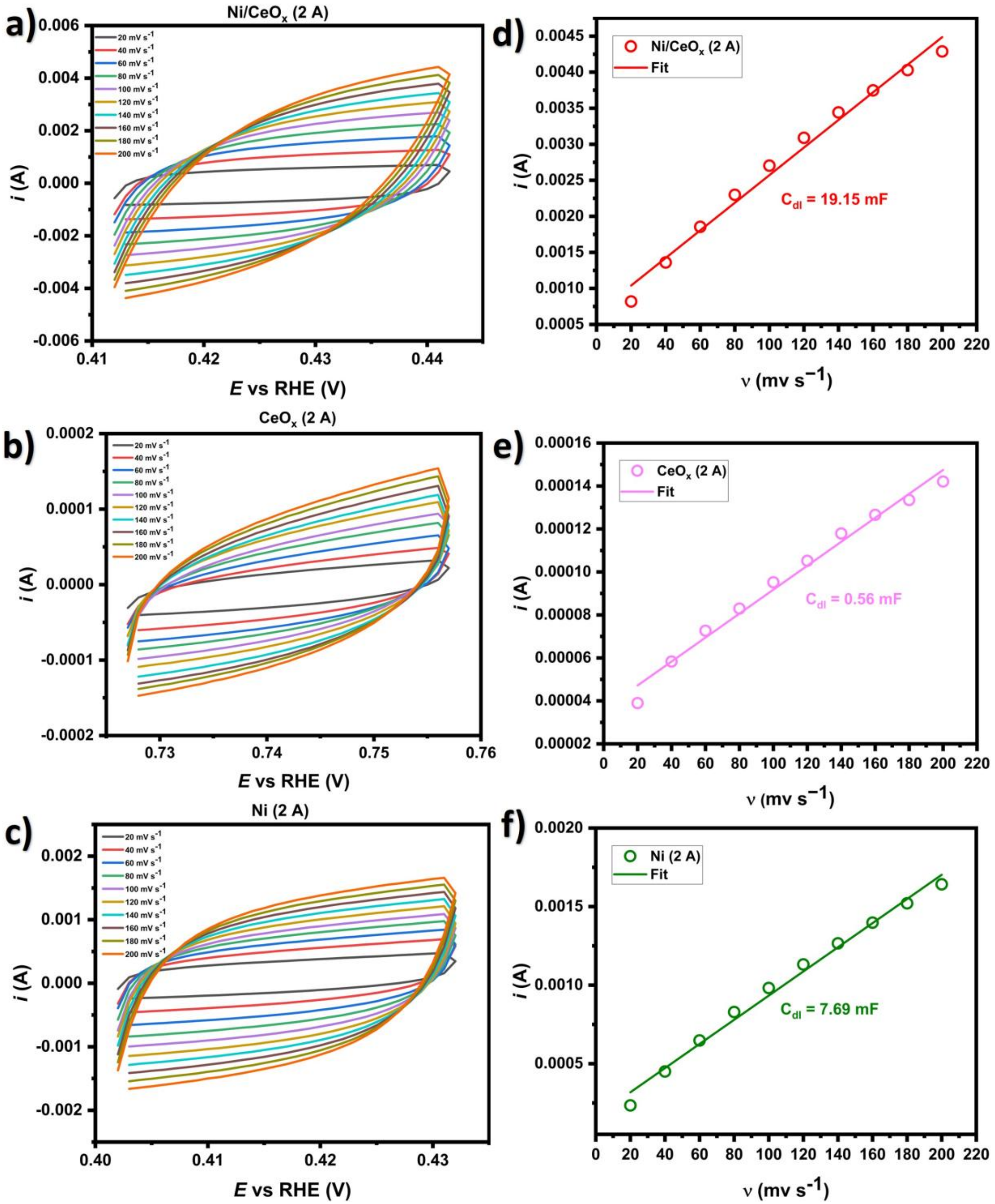

Fig. S18. a-c) Capacitive CVs in 1.0 M KOH at different potential scan rates (10:100 mV s^{-1}). d-f) The variation of capacitive current with potential scan rate for the Ni/CeO$_x$ (2 A), CeO$_x$ (2 A), and Ni (2 A) films.

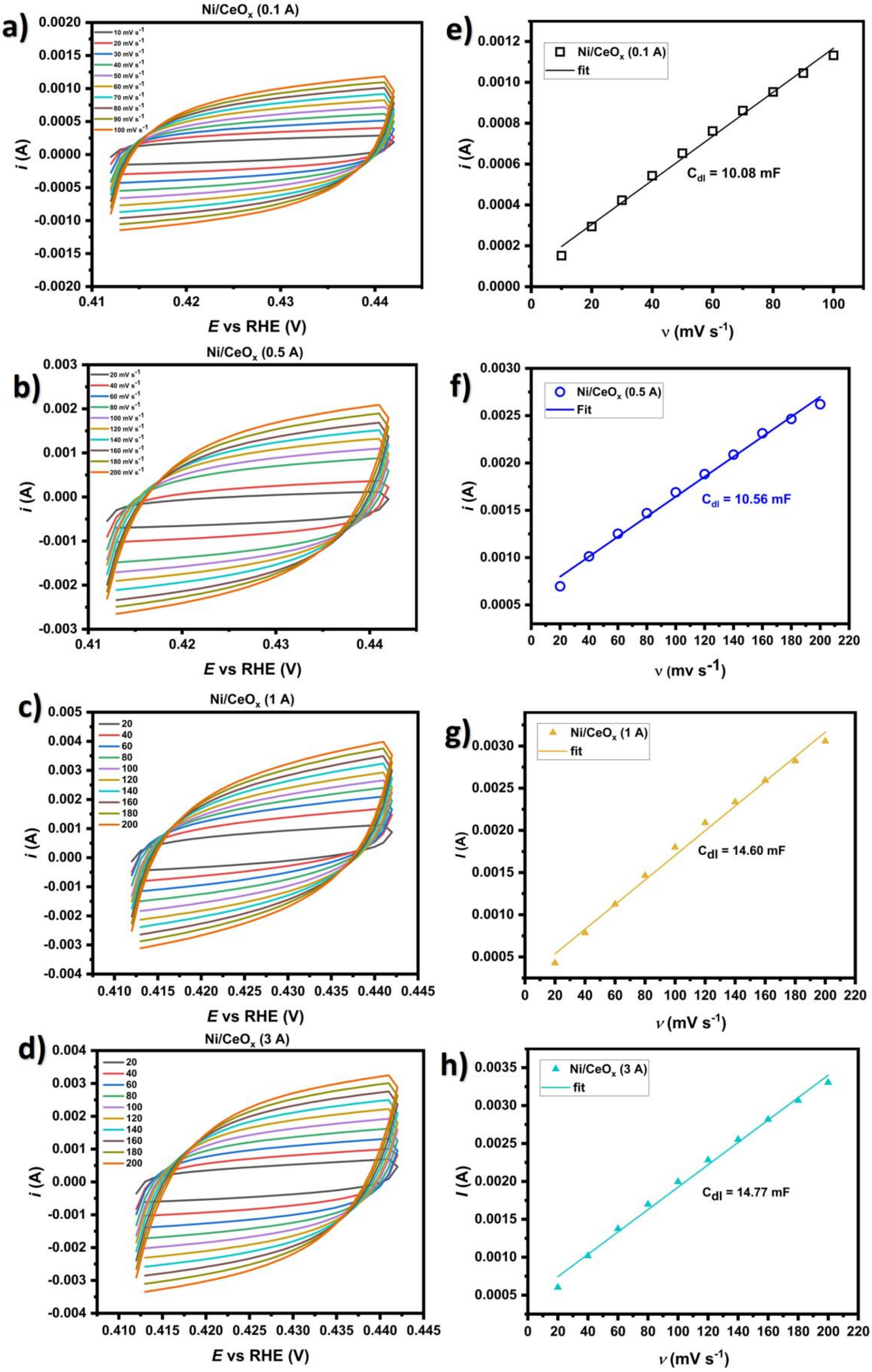

Fig. S19. a-d) Capacitive CVs in 1.0 M KOH at different potential scan rates (10:100 mV s^{-1}). e-h) The variation of capacitive current with potential scan rate for the Ni/CeO$_x$ (0.1 A), Ni/CeO$_x$ (0.5 A), Ni/CeO$_x$ (1 A), and Ni/CeO$_x$ (3 A) films.

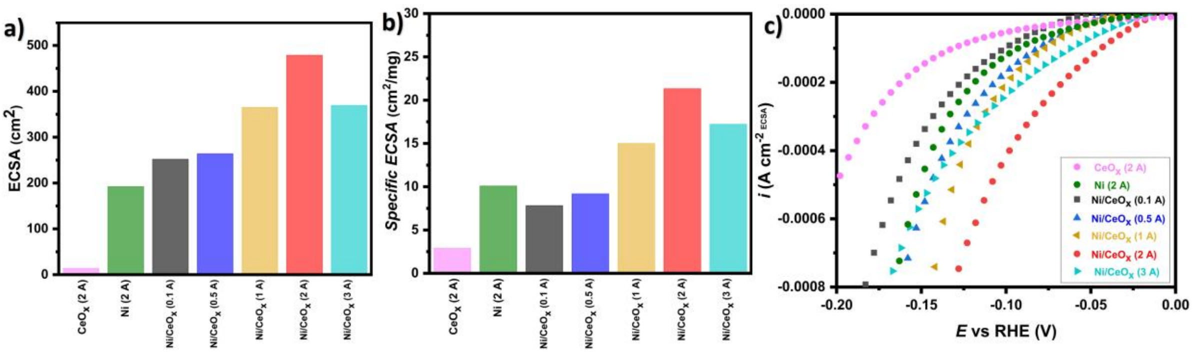

Fig. S20. a) *ECSA* values. b) Specific *ECSA* values. c) LSVs, normalized to ECSA, in 1.0 M KOH at a potential scan rate of 10 mV s^{-1} of the designed electrocatalysts.

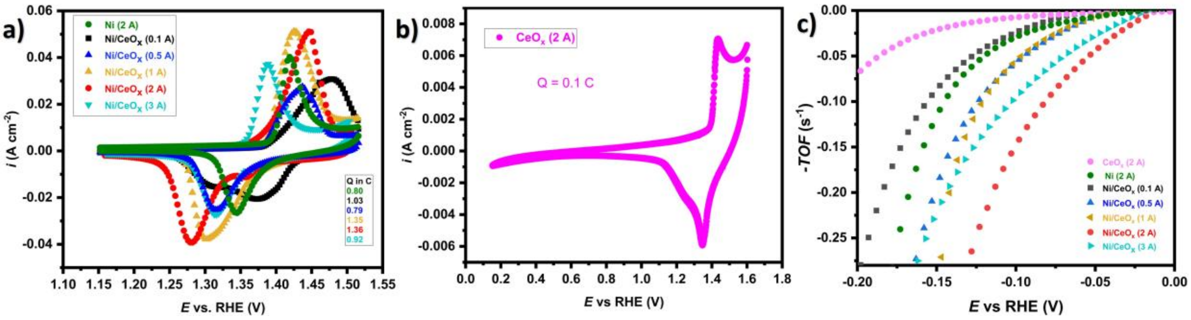

Fig. S21. a-b) CVs of the designed films. b) CV of CeO$_x$ (2 A) film. C) *TOFs* of the designed electrocatalysts.

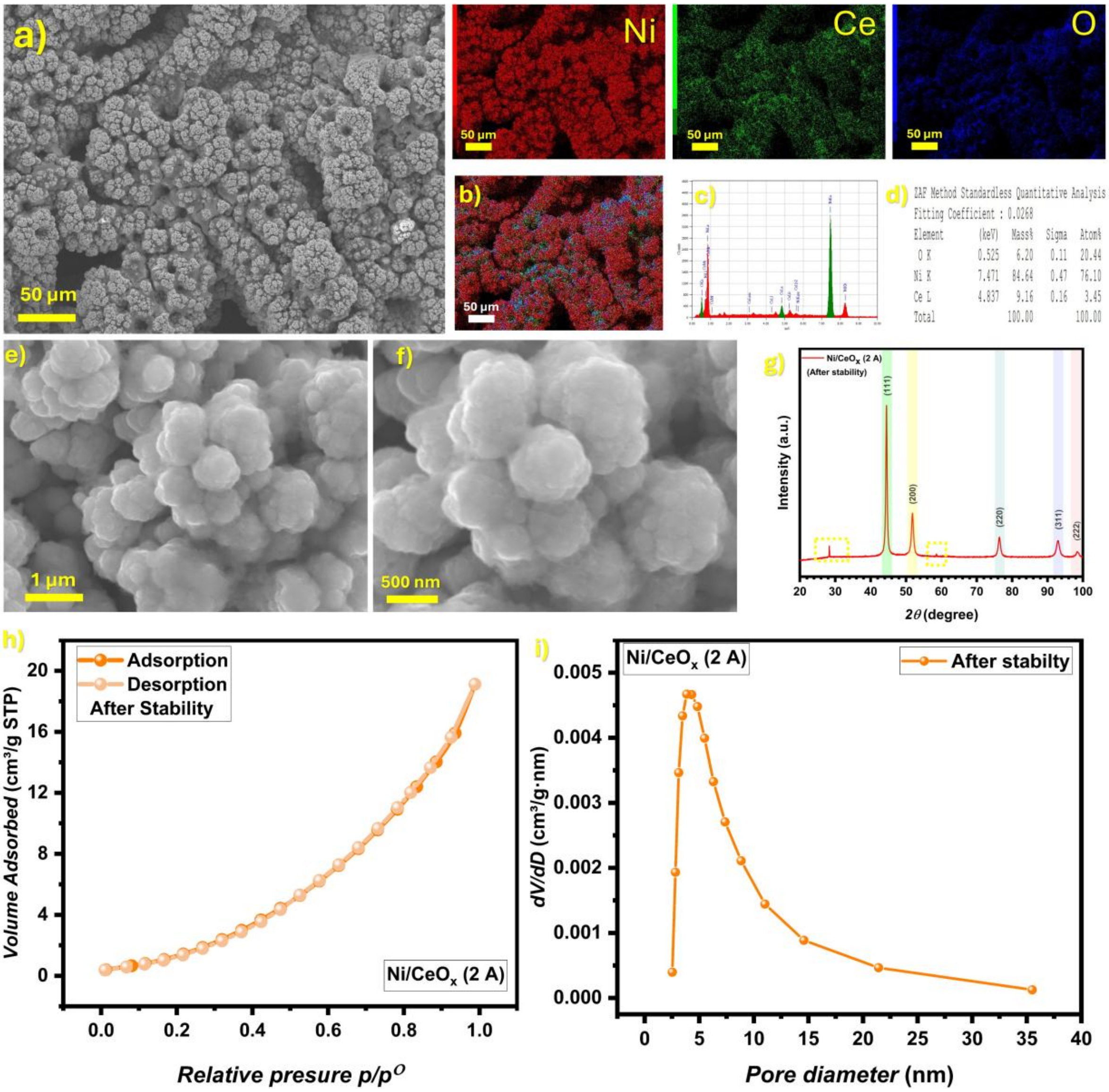

d) ZAF Method Standardless Quantitative Analysis

Fitting Coefficient : 0.0268

Element	(keV)	Mass%	Sigma	Atom%
O K	0.525	6.20	0.11	20.44
Ni K	7.471	84.64	0.47	76.10
Ce L	4.837	9.16	0.16	3.45
Total		100.00		100.00

Fig. S22. After stability a) SEM micrograph and the corresponding EDS elemental mapping, b) overlay, c) spectra, and d) percentages. e-f) Other SEM at different magnifications. g) XRD pattern of the Ni/CeO$_x$ (2 A) film (all after HER operation). h) N_2 adsorption/desorption (BET) isotherm and i) pore size distribution of the Ni/CeO$_x$ (2 A) film after stability.

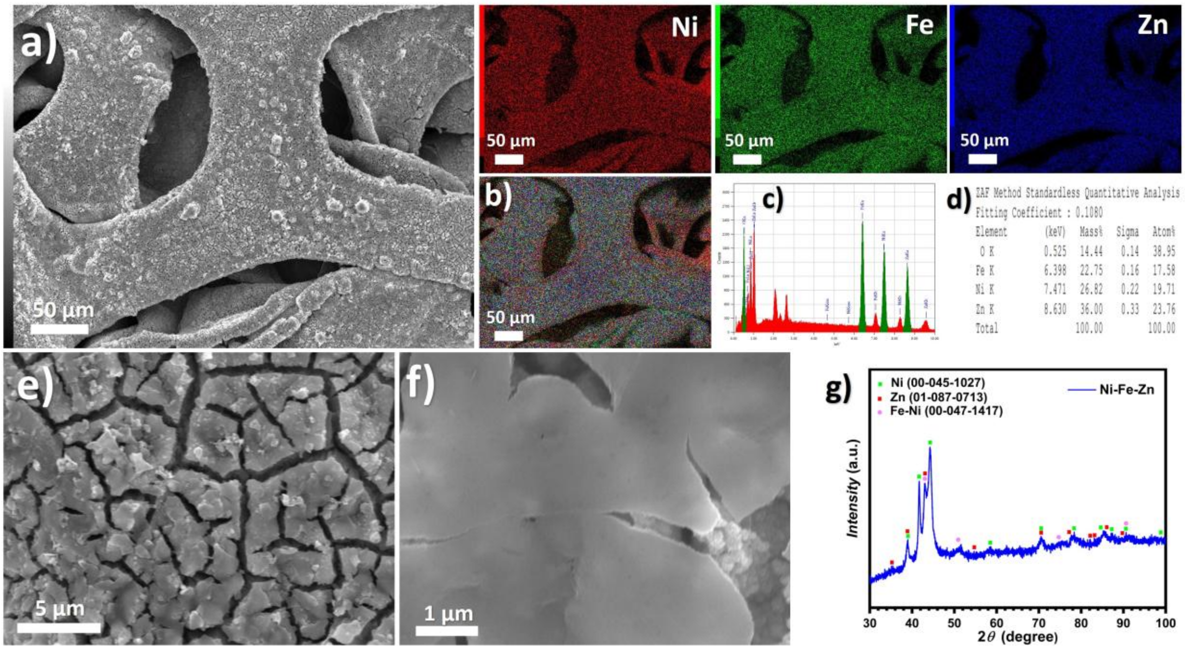

```
ZAF Method Standardless Quantitative Analysis
Fitting Coefficient : 0.1080
Element         (keV)  Mass%  Sigma  Atom%
 O K            0.525  14.44   0.14  38.95
Fe K            6.398  22.75   0.16  17.58
Ni K            7.471  26.82   0.22  19.71
Zn K            8.630  36.00   0.33  23.76
Total                 100.00        100.00
```

Fig. S23. a) SEM micrograph and the corresponding EDS elemental mapping, b) overlay, c) spectra, and d) percentages. e-f) other SEM micrographs at different magnifications. g) XRD pattern of the Ni-Fe-Zn film.

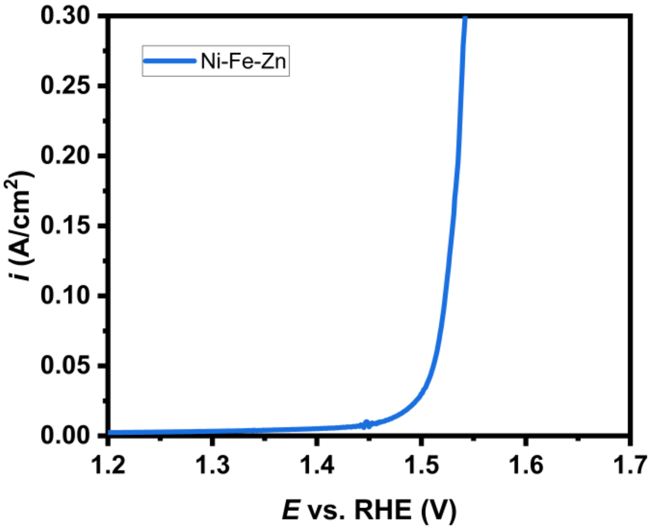

Fig. S24. OER LSV of Ni-Fe-Zn catalyst at 20 °C.

Note S2:

NiFe-based materials have been reported to lead the non-precious electrocatalysts used for OER in alkaline media [13,14]. Herein, a Ni-Fe-Zn OER catalyst is designed, with a near 1:1:1 metal percentage observed from SEM-EDS data (Fig. S23), approaching the molar ratio of precursor ions in the deposition bath. The designed catalyst demonstrates remarkable activity, delivering 300 mA cm^{-2} at an overpotential of 312 mV (Fig. S24), indicating superb OER activity [15,16]. A morphology of cauliflower-like particles wrapped by sheets with various interstitial cracks (Fig. S23e&f) is likely to contribute to the enhanced activity by providing disconnection sites that inhibit oxygen bubble coalescence and reduce mass transfer resistance. The obtained XRD pattern reveals the coexistence of multiple phases (Fig. S23g). The inclusion of Zn^{+2} ions in the deposition bath, and consequently, Zn presence in the designed catalyst, aims to lower the surface roughness of the Ni-Fe catalyst that causes membrane ruption and short circuits when assembled in AEMWE in the absence of Zn. Interestingly, Ni-Fe-Zn shows similar OER performance, while addressing the membrane-related challenges.

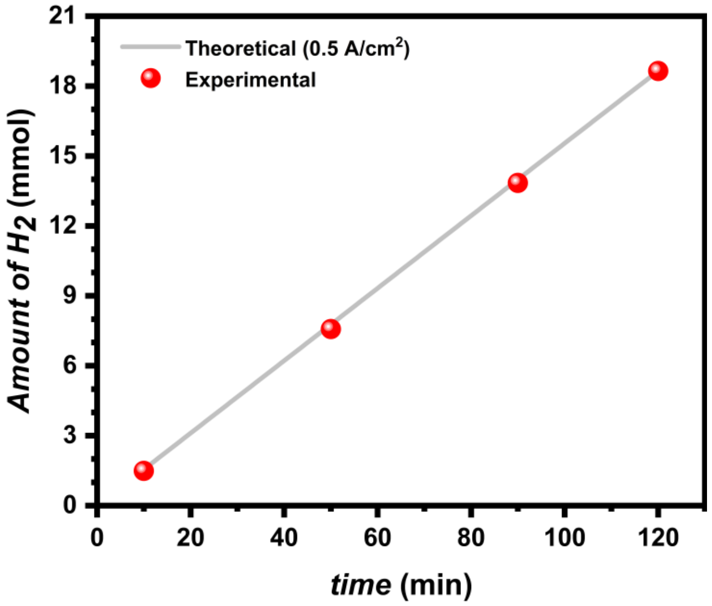

Fig. S25. Theoretical and experimental amount of H_2 product at 0.5 A cm^{-2} in AEMWE.

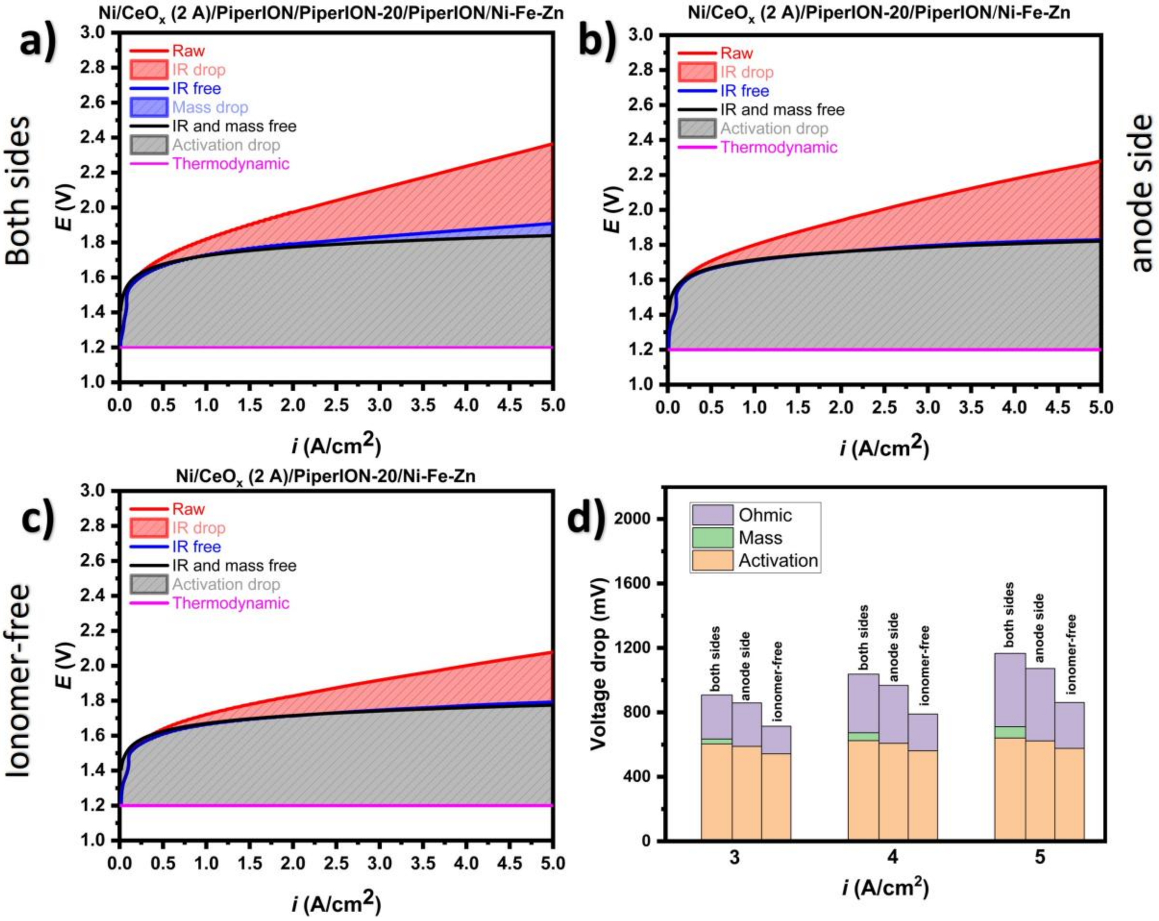

Fig. S26. Deconvoluted LSV of AEMWEs with PiperION-20 membrane at 60 °C when a) PiperION ionomer is at both cathodic and anodic sides. b) at anodic sides only, and c) no PiperION ionomer is added. d) A comparison between the contributing overpotentials at different current densities for the three AEMWE configurations.

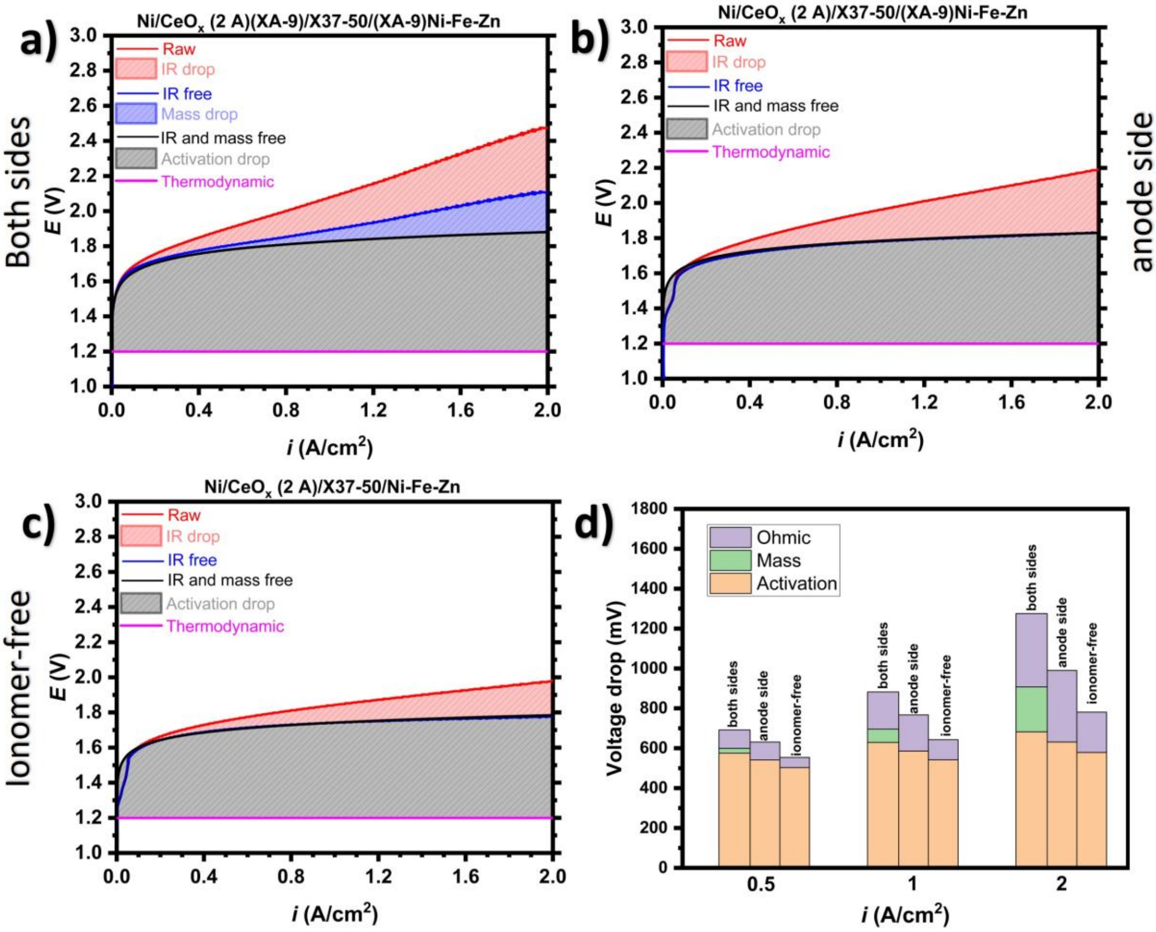

Fig. S27. Deconvoluted LSV of AEMWEs with X37-50 membrane at 60 °C when a) XA-9 ionomer is at both cathodic and anodic sides. b) at anodic sides only, and c) no XA-9 ionomer is added. d) A comparison between the contributing overpotentials at different current densities for the three AEMWE configurations.

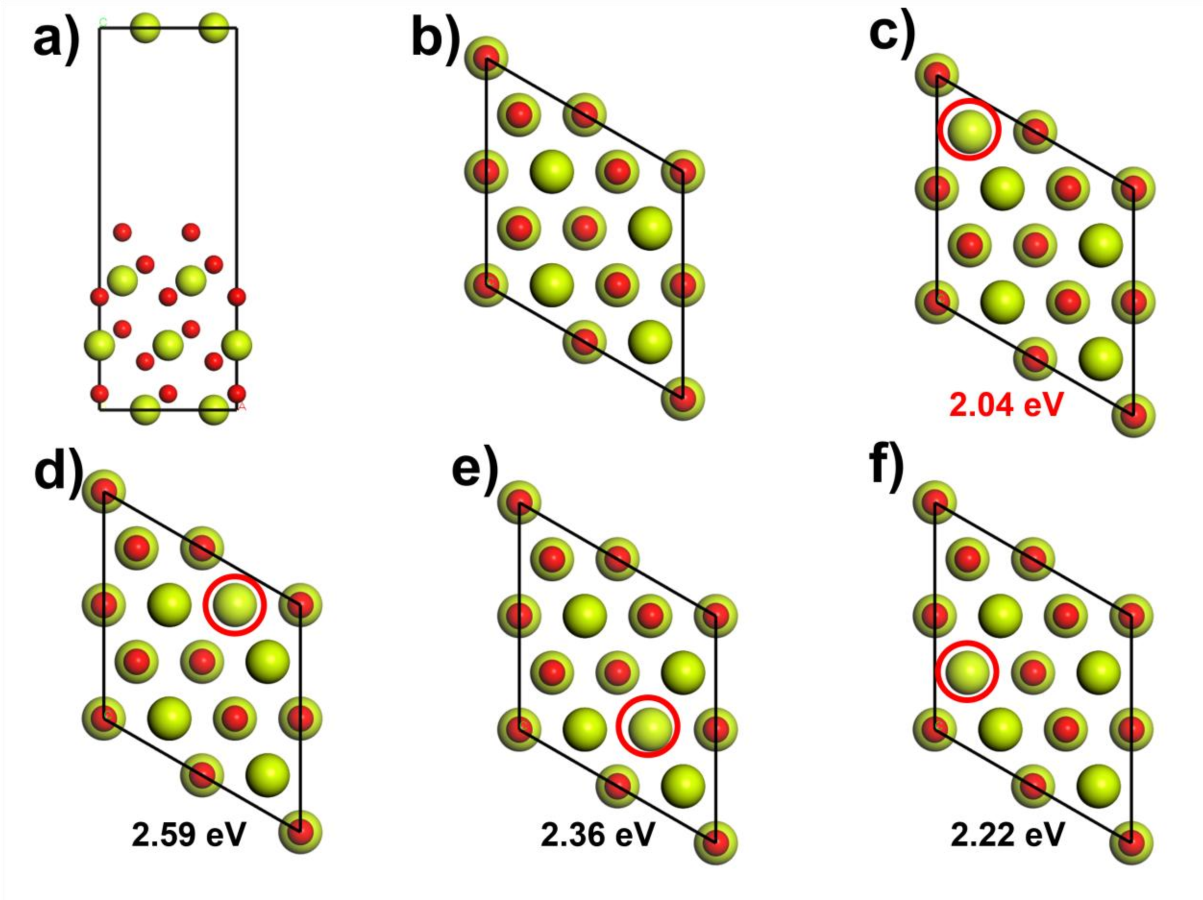

Fig. S28. a) Front view and b) Top view of CeO_2. (c-f) The four possible structures of $CeO_{2-\delta}$ and their corresponding chemical formation energies.

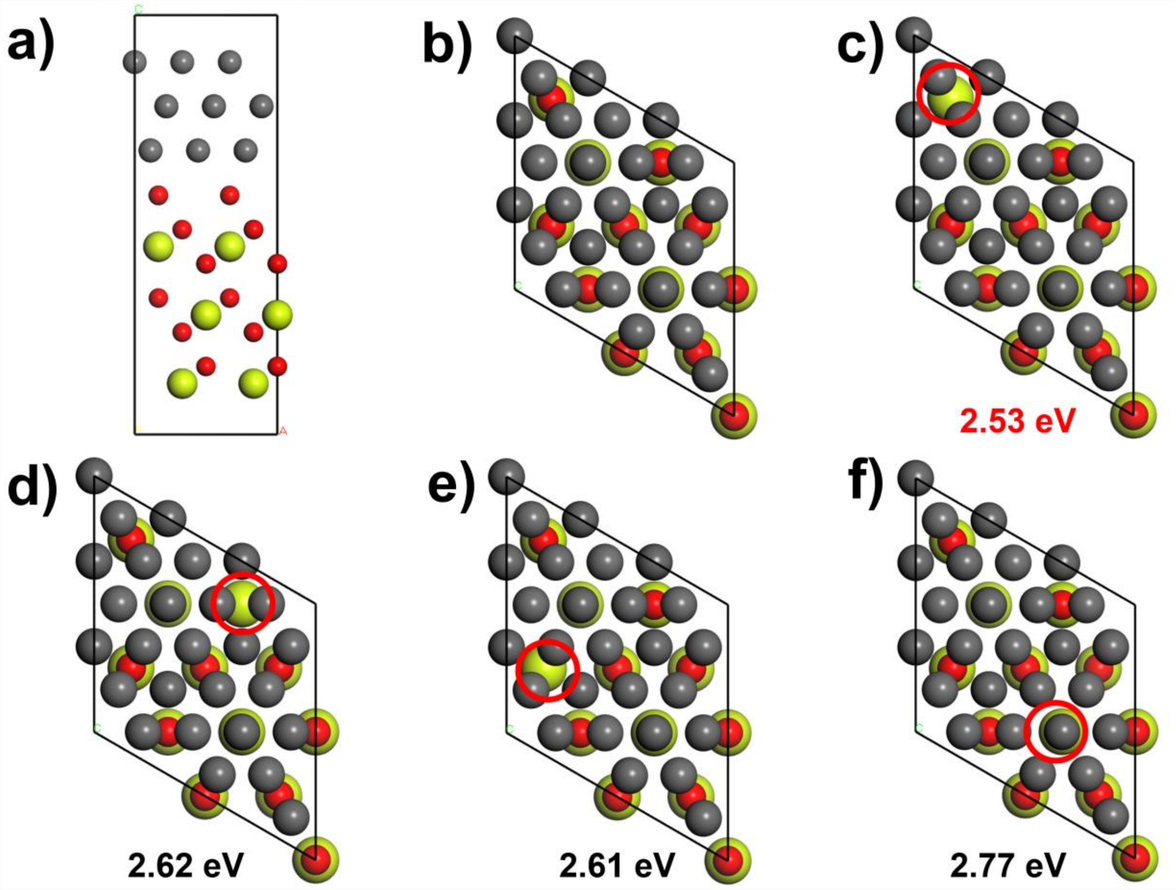

Fig. S29. a) Front view and b) Top view of Ni/CeO_2. (c-f) The four possible structures of Ni/$CeO_{2-\delta}$ and their corresponding chemical formation energies.

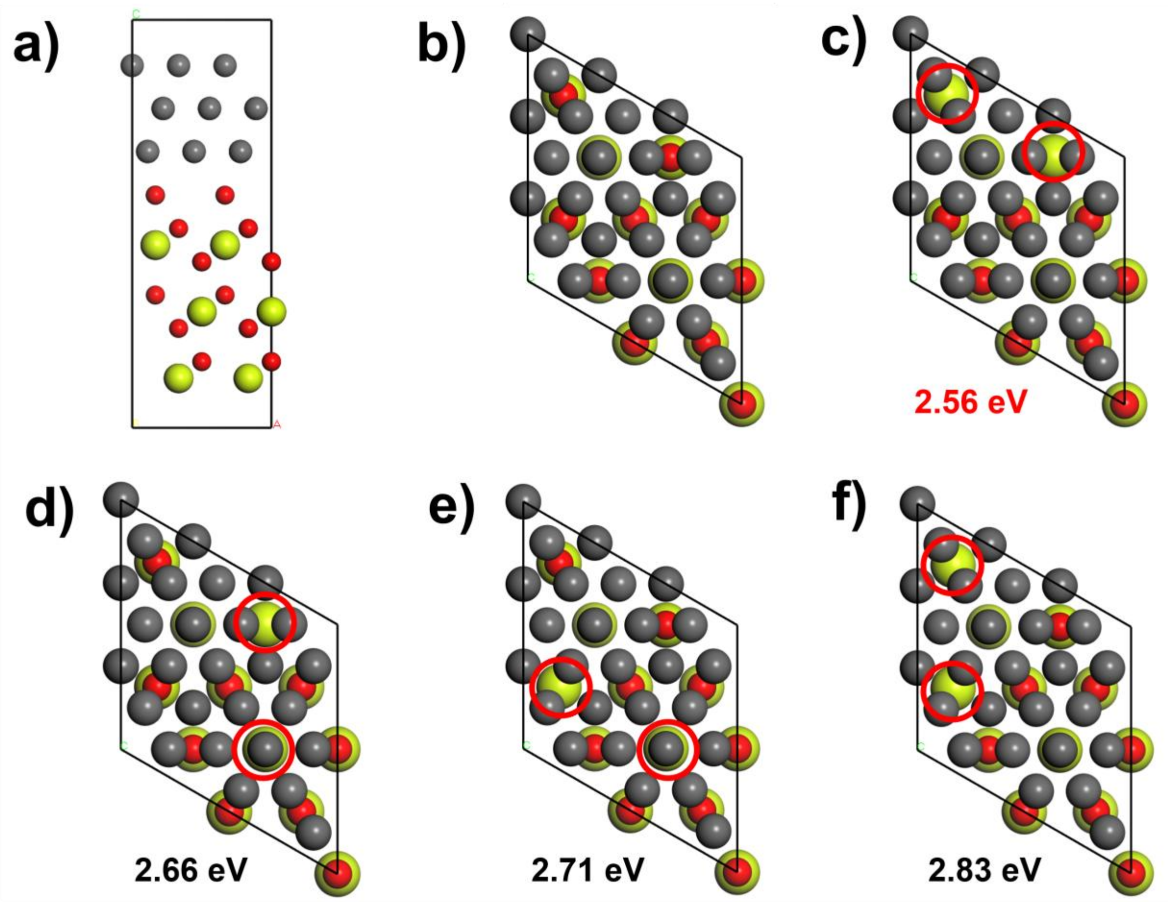

Fig. S30. a) Front view and b) Top view of Ni/CeO_2. (c-f) The four possible structures of Ni/$CeO_{2-2\delta}$ and their corresponding chemical formation energies.

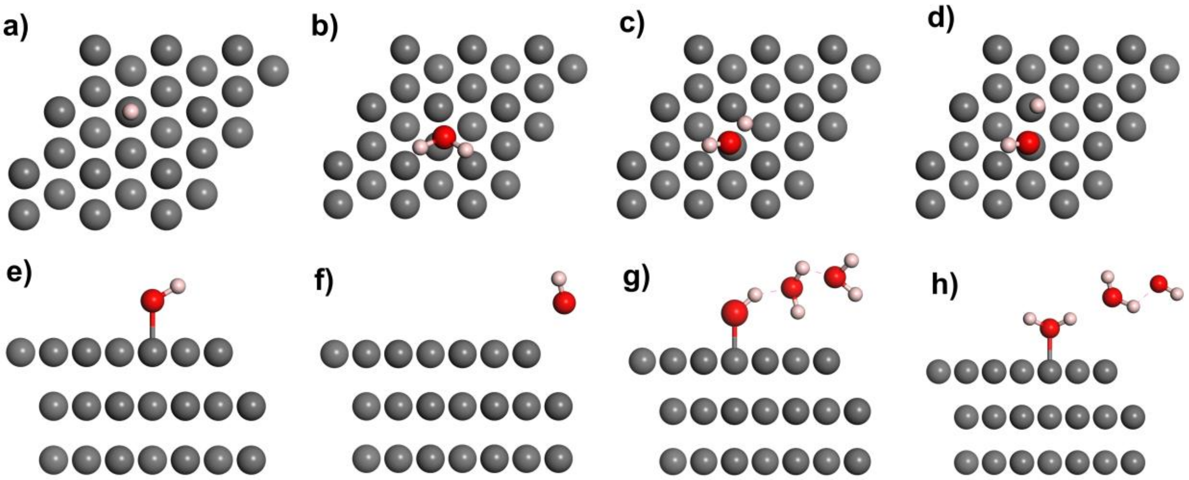

Fig. S31. HER at Ni in alkaline media: a) Hydrogen adsorption. b) IS, c) TS and d) FS of water adsorption and dissociation processes. (e-f) OH* direct desorption process. (g-h) Water-assisted OH* desorption process.

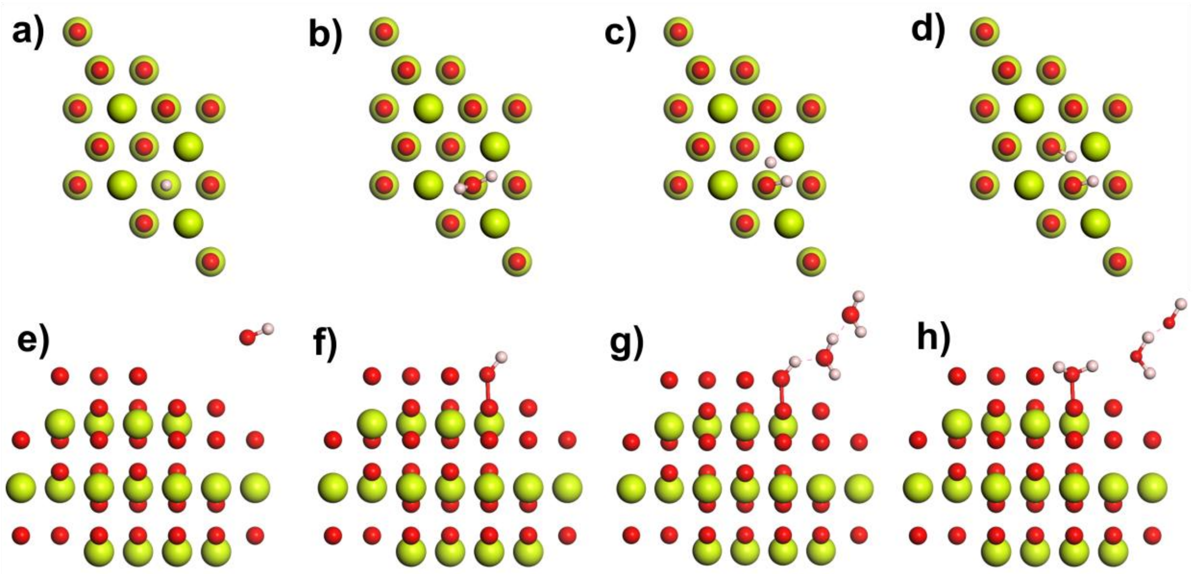

Fig. S32. HER at $CeO_{2-\delta}$ in alkaline media: a) Hydrogen adsorption. b) IS, c) TS and d) FS of water adsorption and dissociation processes. (e-f) OH* direct desorption process. (g-h) Water-assisted OH* desorption process.

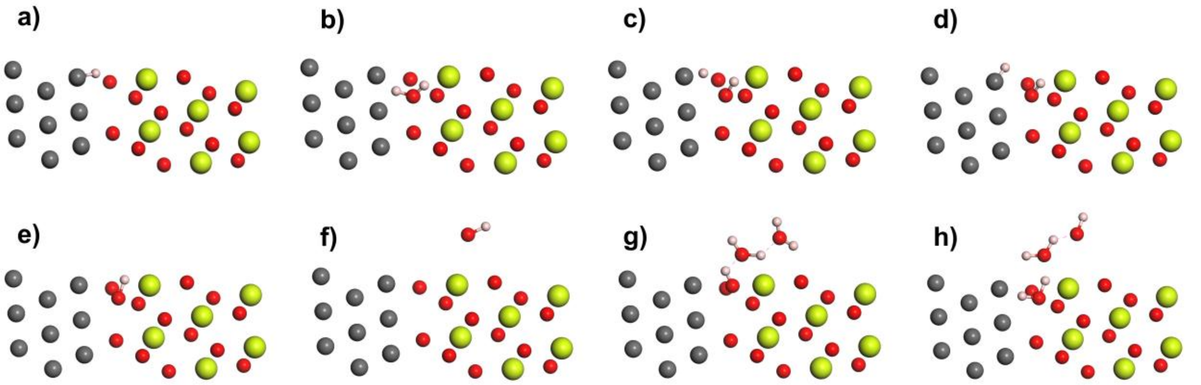

Fig. S33. HER at Ni/$CeO_{2-\delta}$ in alkaline media: a) Hydrogen adsorption. b) IS, c) TS and d) FS of water adsorption and dissociation processes. (e-f) OH* direct desorption process. (g-h) Water-assisted OH* desorption process.

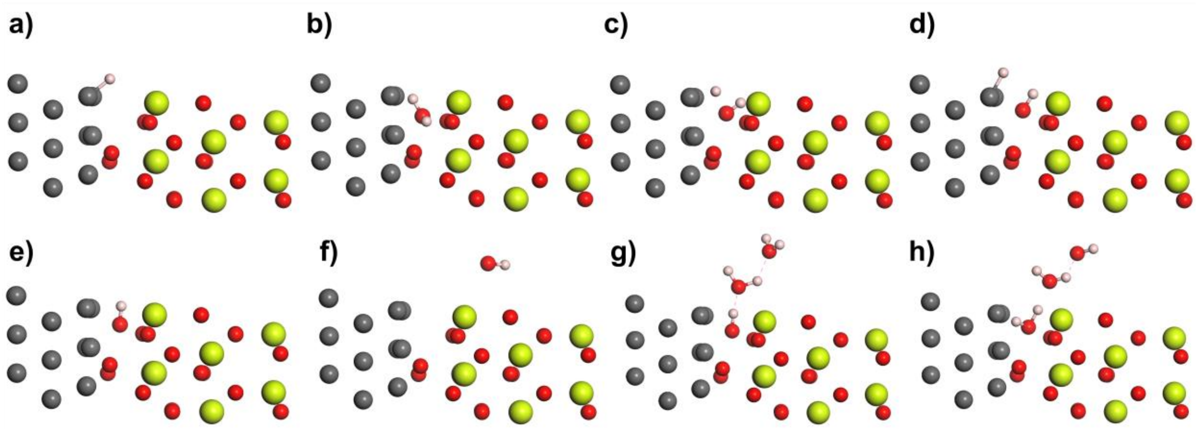

Fig. S34. HER at Ni/CeO$_{2-2\delta}$ in alkaline media: a) Hydrogen adsorption. b) IS, c) TS and d) FS of water adsorption and dissociation process. (e-f) OH* direct desorption process. (g-h) Water-assisted OH* desorption process.

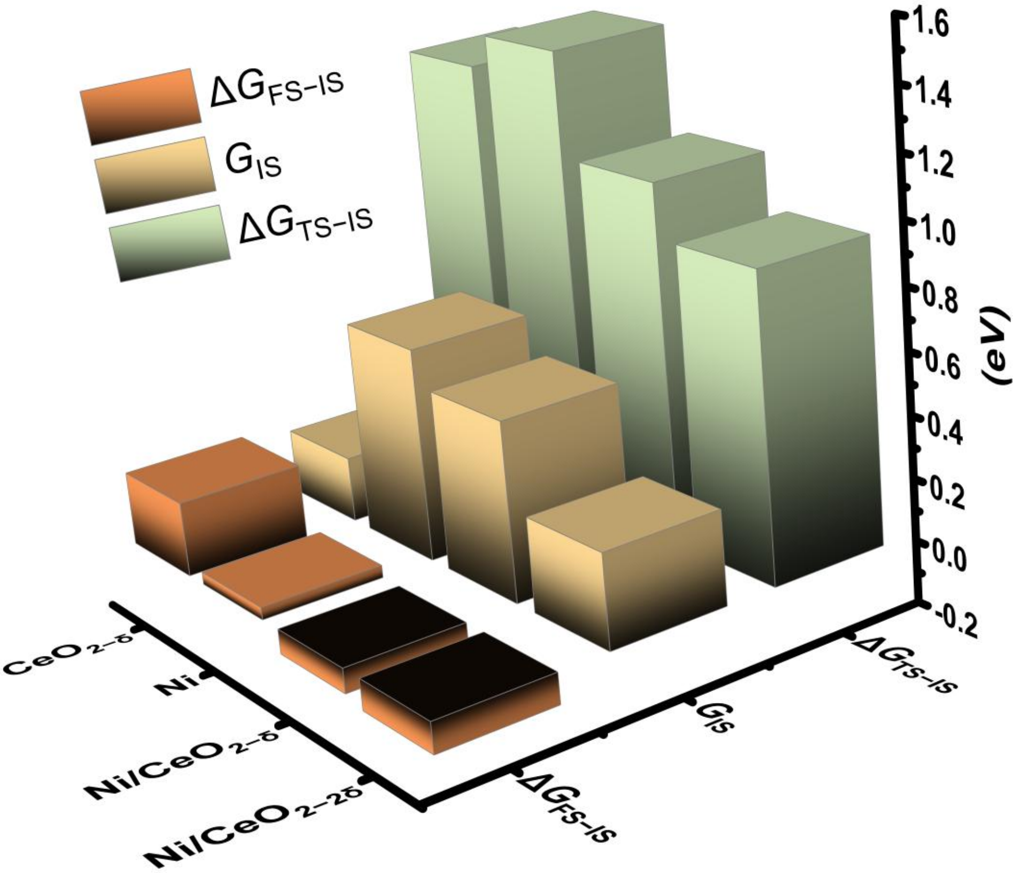

Fig. S35. Trends in Gibbs free energy values for the water dissociation process at $CeO_{2-\delta}$, Ni, $Ni/CeO_{2-\delta}$, and $Ni/CeO_{2-2\delta}$.

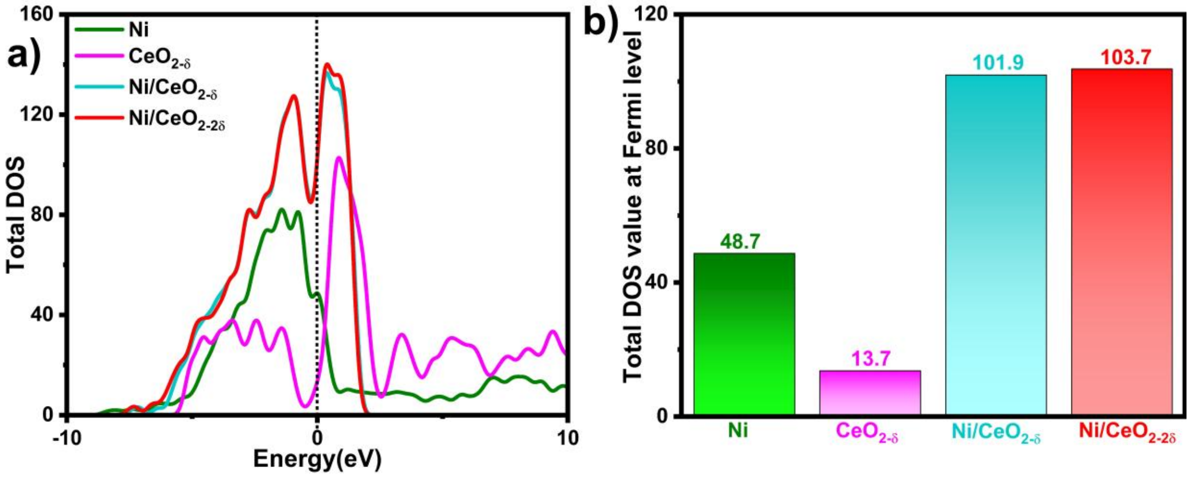

Fig. S36. a) The total DOS plots of Ni, $CeO_{2-\delta}$, Ni/$Ce_{2-\delta}$, and Ni/$Ce_{2-2\delta}$. b) Their total DOS values at the Fermi level.

Table S1. Atomic percentages of Ni and Ce in the designed films, the corresponding total metals mass, and deposition efficiency from ICP-OES data.

Film	Ce atomic %	Ni atomic %	Total metals mass (mg)	Deposition faradaic efficiency %
CeO_x (2 A)	100	-	4.83	0.37
Ni (2 A)	-	100	19.05	6.96
Ni/CeO_x (0.1 A)	0.26	99.74	32.23	11.72
Ni/CeO_x (0.5 A)	3.88	96.12	28.77	9.78
Ni/CeO_x (1 A)	2.91	97.09	24.34	8.42
Ni/CeO_x (2 A)	2.8	97.2	22.45	7.78
Ni/CeO_x (3 A)	3.6	96.4	21.45	7.32

Table S2. XRD cubic Ni peaks' positions for all prepared films.

Facet / Film	111/degree	200/degree	220/degree	311/degree	222/degree
Ni (2 A)	44.50	51.84	76.38	92.92	98.44
Ni/CeO$_x$ (0.1 A)	44.47	51.79	76.42	92.90	98.42
Ni/CeO$_x$ (0.5 A)	44.52	51.94	76.42	92.95	98.53
Ni/CeO$_x$ (1 A)	44.50	51.84	76.42	92.97	98.46
Ni/CeO$_x$ (3 A)	44.39	51.72	76.26	92.88	98.44
Ni/CeO$_x$ (2 A)	44.55	51.86	76.40	92.97	98.45

Table S3. Comparison between the activities of HER electrocatalysts in alkaline media.

Electrocatalyst	Current density (mA)	Overpotential (mV)	Electrolyte	Ref.
Pt/C/NF	1000	590	1.0 M KOH	17
Ni_2P/NF	1000	306	1.0 M KOH	17
Pt/C	700	200	1.0 M KOH	18
Ni-CO-P/NF	1000	300	1.0 M KOH	18
Pt/C	500	295	1.0 M KOH	19
Fe-$Co_{0.85}$Se/FeCo LDH	500	274	1.0 M KOH	19
Co-Mo_5N_6	1000	280	1.0 M KOH	20
Pt/C	1000	650	1.0 M KOH	20
Ni(OH)x/Ni_3S_2/NF	1000	238	1.0 M KOH	21
Pt/NiO_x-O_V/NF	500	180	1.0 M KOH	22
IrNi-$FeNi_3$	1000	289	1.0 M KOH	23
Pt/C/CuF	1000	450	1.0 M KOH	24
$CuMo_6S_8$/Cu	1000	320	1.0 M KOH	24
Co-P	1000	227	1.0 M KOH	25
MoS_2/Mo_2C	1000	220	1.0 M KOH	26
Ni_3S_2/Cr_2S_3@NF	1000	227	1.0 M KOH	27
$Ni_{2(1-x)}Mo_{2x}P$	1000	294	1.0 M KOH	28
Ru-CoO_x/NF	1000	252	1.0 M KOH	29
N-NiMoS	1000	322	1.0 M KOH	30
A-NiCo LDH/NF	1000	381	1.0 M KOH	31
Ni-P-B/NF	1000	275	1.0 M KOH	32
Pd_4S/$Pd_3P_{0.95}$	500	387	1.0 M KOH	33

MnO_x/NiFeP/NF	500	255	1.0 M KOH	34
Mo_2C/MoC/CNT	1000	233	1.0 M KOH	35
FeIr/NF	1000	204	1.0 M KOH	36
P-Mo_2N-CNS	1000	256	1.0 M KOH	37
Ni_3S_2–$NiMoO_4$/NF	1000	257	1.0 M KOH	38
P-Fe_3O_4/IF	1000	240	1.0 M KOH	39
$FeCoNiP_0S_1$	1000	264	1.0 M KOH	40
Fe_2P-Co_2P/CF	1000	254	1.0 M KOH	41
$NiCoS_xSe_y$	1000	345	1.0 M KOH	42
Ni/W_5N_4/NF	1000	291	1.0 M KOH	43
CoRu/NC-700	1000	217	1.0 M KOH	44
Ni/Fe_3O_4/IF	1000	387	1.0 M KOH	45
Ni-FeO_x/$FeNi_3$/NF	1000	272	1.0 M KOH	46
Co-MoS_2/V_2C@CC	1000	296	1.0 M KOH	47
3F-FeP	1000	302	1.0 M KOH	48
NiCoSeP	1000	290	1.0 M KOH	49
H-CoS_x@NiFe LDH/NF	1000	375	1.0 M KOH	50
Ni_5P_4-Co_2P/NCF	1000	267	1.0 M KOH	51
(WO_2-$Ni_{17}W_3$)/$NiFe(OH)_x$	1000	258	1.0 M KOH	52
Fe-Ni_2P@C/NF	1000	313	1.0 M KOH	53
NiMoP	700	390	1.0 M KOH	54
GDY-Pd1	1000	261	1.0 M KOH	55
Ni_2P/$WO_{2.83}$/NF	1000	255	1.0 M KOH	56
Ni/CeO_x (2 A)	1000	201	1.0 M KOH	This work

Table S4. Comparison between the performance of AEMWEs.

System Cathode/ membrane /anode	Current (A)	Voltage (V)	IR-free Voltage (V)	Media	Temp. (°C)	Ref.
NiFe/TP-4/ X37−50 Grade T /NiMo/TP-4	2	2	1.87	1.0 M KOH	50-55	57
Pt@S-NiFe LDH/ FAA-3-PK-130 /S-NiFe LDH	0.2	1.74	-	1.0 M KOH	65	58
Pt/C/ FAA-3-50, Fumapem /$CoSb_2O_6$	0.8	1.9	1.769	1.0 M KOH	60	59
NiCoO-NiCo/C/ X37−50 Grade T /CuCoO	0.504	1.85	-	1.0 M KOH	50	60
Pt/C/ X37−50 Grade T /CF-FeSO	0.1	1.61	-	1.0 M KOH	-	61
Pt/C /Fumasep FAA-3–50 /Ni_2P/Ni_7S_6	0.204	2	1.75	1.0 M KOH	25	62
MOC-Ru/-/RuO2	0.25	1.97	-	1.0 M KOH	Room temp.	63
3-Co_3S_4 NS/NF/ X37−50 /$Cu_{0.81}Co_{2.19}O_4$ NS/NF	0.431	2	-	1.0 M KOH	45-48	64
NiMoCo alloy/ Sustainion X37-FA /NiFeCr-LDH	1	2.11	-	1.0 M KOH	40	65
NiFeS@Ti_3C_2/ X37–50 RT /NiFeS@Ti_3C_2	0.401	1.85	-	1.0 M KOH	50	66
NiFeP_FA_NN/ FAA-3-PE-30 /NiFe_FA_NN	0.5	2	-	1.0 M KOH	60	67
Ni–W-600@CP/ A201 /Ir black/Ti foam	1	2.3	-	1.0 M KOH	50	68
Pt/C/ HoAM Grion 1204 / Mo-CoOOH	1	2.08	-	1.0 M KOH	85	69
NA-Ru_3Ni/C/ X37−50 /NA-Ru_3Ni/C	1	2.048	-	1.0 M KOH	60	70
Pt/C/ X37−50 / $(NiCo)_3Se_4$	2	2	-	1.0 M KOH	60	71
Ni_3N/Ni/Ti mesh/ Fumapem FA-3-50 /$NiFe_2O_4$	0.5	1.88	1.802	1.0 M KOH	55	72
NiMoN/ X37–50 RT / d-(Fe,Ni)OOH	0.5	1.795	-	1.0 M KOH	73	73
Ni/CeO_x (2 A)/ PiperION-20 /Ni-Fe-Zn	5	2.078	1.793	1.0 M KOH	60	This work
	4	2.001	1.772			
	3	1.918	1.746			
Ni/CeO_x (2 A)/ X37−50 Grade T /Ni-Fe-Zn	2	1.981	1.779			
	1	1.843	1.742			
	0.5	1.754	1.703			

Table S5. Lattice parameters of Ni, CeO_2 and Ni/CeO_2.

	a(Å)	**b(Å)**	**c(Å)**	**α(º)**	**β(º)**	**γ(º)**
Ni	3.53425	3.53425	3.53425	90.0000	90.0000	90.0000
CeO_2	5.47472	5.47472	5.47472	90.0000	90.0000	90.0000
Ni/CeO_2	7.61985	7.61985	19.3633	90.0000	90.0000	120.0000

Table S6. Gibbs free energy values for the water dissociation process at $CeO_{2-\delta}$, Ni, Ni/$CeO_{2-\delta}$, and Ni/$CeO_{2-2\delta}$.

	G_{IS} (eV)	ΔG_{TS-IS} (eV)	ΔG_{FS-IS} (eV)
$CeO_{2-\delta}$	0.21	1.36	0.24
Ni	0.68	1.47	0.04
Ni/$CeO_{2-\delta}$	0.57	1.14	− 0.08
Ni/$CeO_{2-2\delta}$	0.3	0.97	− 0.1

Table S7. Representation of the atoms in the DFT model.

Atom	Color	RGB	Radius
Ce	Lime green	209 252 6	1.82
Ni	Grey	109 109 109	1.25
O	Red	254 3 0	0.74
H	Light pink	255 204 204	0.46

References

1. Aldykiewicz, A. J., Davenport, A. J. & Isaacs, H. S. Studies of the formation of cerium-rich protective films using X-ray Absorption near-edge spectroscopy and rotating disk electrode methods. *J. Electrochem. Soc.* **143**, 147 (1996).
2. Liu, F. *et al.* Rational design of better hydrogen evolution electrocatalysts for water splitting: a review. *Adv. Sci.* **9**, 2200307 (2022).
3. Chen, N. *et al.* Plasma-Engineered MoP with nitrogen doping: Electron localization toward efficient alkaline hydrogen evolution. *Appl. Catal. B Environ.* **268**, 118441 (2020).
4. McCrory, C. C. L. *et al.* Benchmarking hydrogen evolving reaction and oxygen evolving reaction electrocatalysts for solar water splitting devices. *J. Am. Chem. Soc.* **137**, 4347–4357 (2015).
5. McCrory, C. C. L., Jung, S., Peters, J. C. & Jaramillo, T. F. Benchmarking heterogeneous electrocatalysts for the oxygen evolution reaction. *J. Am. Chem. Soc.* **135**, 16977–16987 (2013).
6. Yang, Y. *et al.* Anion-exchange membrane water electrolyzers and fuel cells. *Chem. Soc. Rev.* (2022).
7. Liang, Z. *et al.* Modulating the Electronic Structure of Cobalt-Vanadium Bimetal Catalysts for High-Stable Anion Exchange Membrane Water Electrolyzer. *Adv. Mater.* **36**, 2408634 (2024).
8. Wan, L. *et al.* Key components and design strategy of the membrane electrode assembly for alkaline water electrolysis. *Energy Environ. Sci.* **16**, 1384–1430 (2023).
9. Patnaik, P. *Handbook of inorganic chemicals*. vol. 529 (McGraw-Hill New York, 2003).
10. Yang, L., Pang, X., Fox-Rabinovich, G., Veldhuis, S. & Zhitomirsky, I. Electrodeposition of cerium oxide films and composites. *Surf. Coatings Technol.* **206**, 1–7 (2011).
11. Zhang, Q. *et al.* Myriophyllum-like hierarchical TiN@ Ni 3 N nanowire arrays for bifunctional water splitting catalysts. *J. Mater. Chem. A* **4**, 5713–5718 (2016).
12. Xiong, W., Guo, Z., Li, H., Zhao, R. & Wang, X. Rational Bottom-Up Engineering of Electrocatalysts by Atomic Layer Deposition: A Case Study of Fe x Co1–x S y-Based Catalysts for Electrochemical Hydrogen Evolution. *Acs Energy Lett.* **2**, 2778–2785 (2017).
13. Zhao, J., Zhang, J., Li, Z. & Bu, X. Recent Progress on NiFe-Based Electrocatalysts for the Oxygen Evolution Reaction. *Small* **16**, 2003916 (2020).
14. Anantharaj, S., Kundu, S. & Noda, S. "The Fe Effect": A review unveiling the critical roles of Fe in enhancing OER activity of Ni and Co based catalysts. *Nano Energy* **80**, 105514 (2021).
15. Jamesh, M.-I. & Harb, M. Tuning the electronic structure of the earth-abundant electrocatalysts for oxygen evolution reaction (OER) to achieve efficient alkaline water splitting–A review. *J. Energy Chem.* **56**, 299–342 (2021).
16. Jamesh, M.-I. & Sun, X. Recent progress on earth abundant electrocatalysts for oxygen evolution reaction (OER) in alkaline medium to achieve efficient water splitting–A review. *J. Power Sources* **400**, 31–68 (2018).
17. Yu, X. *et al.* "Superaerophobic" nickel phosphide nanoarray catalyst for efficient hydrogen evolution at ultrahigh current densities. *J. Am. Chem. Soc.* **141**, 7537–7543 (2019).
18. Yu, C. *et al.* Bimetallic Ni–Co phosphide nanosheets self-supported on nickel foam as high-performance electrocatalyst for hydrogen evolution reaction. *Electrochim. Acta* **317**, 191–198 (2019).

19. Yu, H. *et al.* Modulating Local Interfacial Bonding Environment of Heterostructures for Energy-Saving Hydrogen Production at High Current Densities. *Adv. Funct. Mater.* **33**, 2212811 (2023).
20. Lin, F. *et al.* Electrocatalytic hydrogen evolution of ultrathin Co-Mo5N6 heterojunction with interfacial electron redistribution. *Adv. Energy Mater.* **10**, 2002176 (2020).
21. He, W. *et al.* Super-Hydrophilic Microporous Ni (OH) x/Ni3S2 Heterostructure Electrocatalyst for Large-Current-Density Hydrogen Evolution. *Small* **19**, 2205719 (2023).
22. Wang, K. *et al.* Dense Platinum/Nickel Oxide Heterointerfaces with Abundant Oxygen Vacancies Enable Ampere-Level Current Density Ultrastable Hydrogen Evolution in Alkaline. *Adv. Funct. Mater.* **33**, 2211273 (2023).
23. Wang, Y. *et al.* Industrially promising IrNi-FeNi3 hybrid nanosheets for overall water splitting catalysis at large current density. *Appl. Catal. B Environ.* **286**, 119881 (2021).
24. Liu, H. *et al.* Dual interfacial engineering of a Chevrel phase electrode material for stable hydrogen evolution at 2500 mA cm− 2. *Nat. Commun.* **13**, 1–10 (2022).
25. Jiang, N., You, B., Sheng, M. & Sun, Y. Electrodeposited cobalt-phosphorous-derived films as competent bifunctional catalysts for overall water splitting. *Angew. Chemie* **127**, 6349–6352 (2015).
26. Luo, Y. *et al.* Morphology and surface chemistry engineering toward pH-universal catalysts for hydrogen evolution at high current density. *Nat. Commun.* **10**, 269 (2019).
27. Fu, H. Q. *et al.* Hydrogen spillover-bridged Volmer/Tafel processes enabling ampere-level current density alkaline hydrogen evolution reaction under low overpotential. *J. Am. Chem. Soc.* **144**, 6028–6039 (2022).
28. Yu, L. *et al.* Ternary Ni2 (1-x) Mo2xP nanowire arrays toward efficient and stable hydrogen evolution electrocatalysis under large-current-density. *Nano Energy* **53**, 492–500 (2018).
29. Wu, D., Chen, D., Zhu, J. & Mu, S. Ultralow Ru incorporated amorphous cobalt-based oxides for high-current-density overall water splitting in alkaline and seawater media. *Small* **17**, 2102777 (2021).
30. Huang, C. *et al.* N-doped Ni-Mo based sulfides for high-efficiency and stable hydrogen evolution reaction. *Appl. Catal. B Environ.* **276**, 119137 (2020).
31. Yang, H., Chen, Z., Guo, P., Fei, B. & Wu, R. B-doping-induced amorphization of LDH for large-current-density hydrogen evolution reaction. *Appl. Catal. B Environ.* **261**, 118240 (2020).
32. Hao, W. *et al.* Fabrication of practical catalytic electrodes using insulating and eco-friendly substrates for overall water splitting. *Energy Environ. Sci.* **13**, 102–110 (2020).
33. Zhang, G. *et al.* Interfacial engineering to construct antioxidative Pd4S/Pd3P0. 95 heterostructure for robust hydrogen production at high current density. *Adv. Energy Mater.* **12**, 2103511 (2022).
34. Wang, P. *et al.* MnOx-Decorated Nickel-Iron Phosphides Nanosheets: Interface Modifications for Robust Overall Water Splitting at Ultra-High Current Densities. *Small* **18**, 2105803 (2022).
35. Li, C. *et al.* Ultrafast self-heating synthesis of robust heterogeneous nanocarbides for high current density hydrogen evolution reaction. *Nat. Commun.* **13**, 3338 (2022).
36. Shen, F. *et al.* Bimetallic iron-iridium alloy nanoparticles supported on nickel foam as highly efficient and stable catalyst for overall water splitting at large current density. *Appl. Catal. B Environ.* **278**, 119327 (2020).
37. Wang, Q. *et al.* Free-standing phosphorous-doped molybdenum nitride in 3D carbon

nanosheet towards hydrogen evolution at all pH values. *J. Energy Chem.* **50**, 44–51 (2020).

38. Zhuo, X. *et al.* Crystalline–Amorphous Ni3S2–NiMoO4 Heterostructure for Durable Urea Electrolysis-Assisted Hydrogen Production at High Current Density. *ACS Appl. Mater. Interfaces* **14**, 46481–46490 (2022).
39. Zhang, J. *et al.* Modulation of inverse spinel Fe3O4 by phosphorus doping as an industrially promising electrocatalyst for hydrogen evolution. *Adv. Mater.* **31**, 1905107 (2019).
40. Wang, X. *et al.* Amorphous multi-elements electrocatalysts with tunable bifunctionality toward overall water splitting. *ACS Catal.* **8**, 9926–9935 (2018).
41. Liu, X. *et al.* In situ-grown cobalt–iron phosphide-based integrated electrode for long-term water splitting under a large current density at the industrial electrolysis temperature. *ACS Sustain. Chem. Eng.* **8**, 17828–17838 (2020).
42. Ma, S. *et al.* One-step in-situ sprouting high-performance NiCoSxSey bifunctional catalysts for water electrolysis at low cell voltages and high current densities. *Chem. Eng. J.* **435**, 134859 (2022).
43. Zhou, Y. *et al.* Surface reconstruction and charge distribution enabling Ni/W5N4 Mott-Schottky heterojunction bifunctional electrocatalyst for efficient urea-assisted water electrolysis at a large current density. *Appl. Catal. B Environ.* **323**, 122168 (2023).
44. Chen, J. *et al.* Enhancing the electronic metal-support interaction of CoRu alloy and pyridinic N for electrocatalytic pH-universal hydrogen evolution reaction. *Chem. Eng. J.* **450**, 138026 (2022).
45. Xu, W. *et al.* Tailoring interfacial electron redistribution of Ni/Fe3O4 electrocatalysts for superior overall water splitting. *J. Energy Chem.* **73**, 330–338 (2022).
46. Qayum, A. *et al.* Highly Durable and Efficient Ni-FeO x/FeNi3 Electrocatalysts Synthesized by a Facile In Situ Combustion-Based Method for Overall Water Splitting with Large Current Densities. *ACS Appl. Mater. Interfaces* **14**, 27842–27853 (2022).
47. Chen, Y. *et al.* Interfacial engineering of Co-doped 1T-MoS2 coupled with V2C MXene for efficient electrocatalytic hydrogen evolution. *Chem. Eng. J.* **450**, 138157 (2022).
48. Zhang, X.-Y. *et al.* Tailoring the d-band centers of FeP nanobelt arrays by fluorine doping for enhanced hydrogen evolution at high current density. *Fuel* **316**, 123206 (2022).
49. Maleki, M., Sabour Rouhaghdam, A., Barati Darband, G., Han, D. & Shanmugam, S. Highly active and durable NiCoSeP nanostructured electrocatalyst for large-current-density hydrogen production. *ACS Appl. Energy Mater.* **5**, 2937–2948 (2022).
50. Lee, Y. J. & Park, S. Metal–Organic Framework-Derived Hollow CoSx Nanoarray Coupled with NiFe Layered Double Hydroxides as Efficient Bifunctional Electrocatalyst for Overall Water Splitting. *Small* **18**, 2200586 (2022).
51. Ma, S. *et al.* Compositional and crystallographic design of Ni-Co phosphide heterointerfaced nanowires for high-rate, stable hydrogen generation at industry-relevant electrolysis current densities. *Nano Energy* **95**, 106989 (2022).
52. Liu, J. *et al.* Amorphous-crystalline heterostructure for simulated practical water splitting at high-current–density. *Chem. Eng. J.* **431**, 134247 (2022).
53. Li, D. *et al.* Coupling overall water splitting and biomass oxidation via Fe-doped Ni2P@ C nanosheets at large current density. *Appl. Catal. B Environ.* **307**, 121170 (2022).
54. Mandavkar, R. *et al.* Electron enriched ternary NiMoB electrocatalyst for improved overall water splitting: Better performance as compared to the Pt/C|| RuO2 at high

current density. *Appl. Mater. Today* **29**, 101579 (2022).

55. Zhang, D. *et al.* Controlled growth of single-crystal Pd quantum dots on 2D carbon for large current density hydrogen evolution. *Adv. Funct. Mater.* **32**, 2111501 (2022).
56. Zhou, Y. *et al.* Heterointerface and defect dual engineering in a superhydrophilic Ni2P/WO2. 83 microsphere for boosting alkaline hydrogen evolution reaction at high current density. *ACS Appl. Mater. Interfaces* **14**, 18816–18824 (2022).
57. Oh, J. H. *et al.* Self-supported electrodes to enhance mass transfer for high-performance anion exchange membrane water electrolyzer. *Chem. Eng. J.* **460**, 141727 (2023).
58. Lei, H., Wan, Q., Tan, S., Wang, Z. & Mai, W. Pt-Quantum-Dot-Modified Sulfur-Doped NiFe Layered Double Hydroxide for High-Current-Density Alkaline Water Splitting at Industrial Temperature. *Adv. Mater.* **35**, 2208209 (2023).
59. Ham, K., Hong, S., Kang, S., Cho, K. & Lee, J. Extensive active-site formation in trirutile CoSb2O6 by oxygen vacancy for oxygen evolution reaction in anion exchange membrane water splitting. *ACS Energy Lett.* **6**, 364–370 (2021).
60. Park, Y. S. *et al.* Commercial anion exchange membrane water electrolyzer stack through non-precious metal electrocatalysts. *Appl. Catal. B Environ.* **292**, 120170 (2021).
61. Lee, W. H. *et al.* Electrode reconstruction strategy for oxygen evolution reaction: maintaining Fe-CoOOH phase with intermediate-spin state during electrolysis. *Nat. Commun.* **13**, 605 (2022).
62. Wang, F.-L. *et al.* Porous heterojunction of Ni2P/Ni7S6 with high crystalline phase and superior conductivity for industrial anion exchange membrane water electrolysis. *Appl. Catal. B Environ.* **330**, 122633 (2023).
63. Yang, C. *et al.* Mn-Oxygen Compounds Coordinated Ruthenium Sites with Deprotonated and Low Oxophilic Microenvironments for Membrane Electrolyzer-based H2-Production. *Adv. Mater.* 2303331 (2023).
64. Park, Y. S. *et al.* Co3S4 nanosheets on Ni foam via electrodeposition with sulfurization as highly active electrocatalysts for anion exchange membrane electrolyzer. *Int. J. Hydrogen Energy* **45**, 36–45 (2020).
65. Wang, M. H. *et al.* Operando High-Valence Cr-Modified NiFe Hydroxides for Water Oxidation. *Small* **18**, 2200303 (2022).
66. Chanda, D. *et al.* Effect of the interfacial electronic coupling of nickel-iron sulfide nanosheets with layer Ti3C2 MXenes as efficient bifunctional electrocatalysts for anion-exchange membrane water electrolysis. *Appl. Catal. B Environ.* **321**, 122039 (2023).
67. Wei, Z., Guo, M. & Zhang, Q. Scalable electrodeposition of NiFe-based electrocatalysts with self-evolving multi-vacancies for high-performance industrial water electrolysis. *Appl. Catal. B Environ.* **322**, 122101 (2023).
68. Li, Y. *et al.* Ni17W3–W Interconnected Hybrid Prepared by Atmosphere-and Thermal-Induced Phase Separation for Efficient Electrocatalysis of Alkaline Hydrogen Evolution. *Small* **16**, 2005184 (2020).
69. Tang, L. *et al.* Three-dimensional CoOOH nanoframes confining high-density Mo single atoms for large-current-density oxygen evolution. *J. Mater. Chem. A* **10**, 6242–6250 (2022).
70. Gao, L. *et al.* Engineering a local potassium cation concentrated microenvironment toward the ampere-level current density hydrogen evolution reaction. *Energy Environ. Sci.* (2023).
71. Abed, J. *et al.* In situ formation of nano ni–co oxyhydroxide enables water oxidation electrocatalysts durable at high current densities. *Adv. Mater.* **33**, 2103812 (2021).

72. Zhang, D. *et al.* Unconventional direct synthesis of Ni 3 N/Ni with N-vacancies for efficient and stable hydrogen evolution. *Energy Environ. Sci.* **15**, 185–195 (2022).
73. Wu, L. *et al.* Boosting oxygen evolution reaction of (Fe, Ni) OOH via defect engineering for anion exchange membrane water electrolysis under industrial conditions. *Adv. Mater.* **35**, 2306097 (2023).